

## KEPLER-413B: A SLIGHTLY MISALIGNED, NEPTUNE-SIZE TRANSITING CIRCUMBINARY PLANET

V. B. KOSTOV<sup>1,2,12</sup>, P. R. McCULLOUGH<sup>1,2</sup>, J. A. CARTER<sup>3,13</sup>, M. DELEUIL<sup>4</sup>, R. F. DÍAZ<sup>4</sup>, D. C. FABRYCKY<sup>5</sup>,  
G. HÉBRARD<sup>6,7</sup>, T. C. HINSE<sup>8,9</sup>, T. MAZEH<sup>10</sup>, J. A. OROSZ<sup>11</sup>, Z. I. TSVETANOV<sup>1</sup>, AND W. F. WELSH<sup>11</sup>

<sup>1</sup> Department of Physics and Astronomy, Johns Hopkins University, 3400 North Charles Street, Baltimore, MD 21218, USA; [vkostov@pha.jhu.edu](mailto:vkostov@pha.jhu.edu)

<sup>2</sup> Space Telescope Science Institute, 3700 San Martin Dr., Baltimore, MD 21218, USA

<sup>3</sup> Harvard-Smithsonian Center for Astrophysics, 60 Garden Street, Cambridge, MA 02138, USA

<sup>4</sup> Laboratoire d’Astrophysique de Marseille, 38 rue Frédéric Joliot-Curie, F-13388 Marseille cedex 13, France

<sup>5</sup> Department of Astronomy and Astrophysics, University of Chicago, 5640 South Ellis Avenue, Chicago, IL 60637, USA

<sup>6</sup> Institut d’Astrophysique de Paris, UMR 7095 CNRS, Université Pierre & Marie Curie, 98 bis boulevard Arago, F-75014 Paris, France

<sup>7</sup> Observatoire de Haute-Provence, Université d’Aix-Marseille & CNRS, F-04870 Saint Michel l’Observatoire, France

<sup>8</sup> Korea Astronomy and Space Science Institute (KASI), Advanced Astronomy and Space Science Division, Daejeon 305-348, Republic of Korea

<sup>9</sup> Armagh Observatory, College Hill, BT61 9DG Armagh, NI, UK

<sup>10</sup> Department of Astronomy and Astrophysics, Tel Aviv University, 69978 Tel Aviv, Israel

<sup>11</sup> Department of Astronomy, San Diego State University, 5500 Campanile Drive, San Diego, CA 92182, USA

Received 2013 October 10; accepted 2014 January 22; published 2014 February 26

### ABSTRACT

We report the discovery of a transiting,  $R_p = 4.347 \pm 0.099 R_\oplus$ , circumbinary planet (CBP) orbiting the *Kepler*  $K+M$  eclipsing binary (EB) system KIC 12351927 (Kepler-413) every  $\sim 66$  days on an eccentric orbit with  $a_p = 0.355 \pm 0.002$  AU,  $e_p = 0.118 \pm 0.002$ . The two stars, with  $M_A = 0.820 \pm 0.015 M_\odot$ ,  $R_A = 0.776 \pm 0.009 R_\odot$  and  $M_B = 0.542 \pm 0.008 M_\odot$ ,  $R_B = 0.484 \pm 0.024 R_\odot$ , respectively, revolve around each other every  $10.11615 \pm 0.00001$  days on a nearly circular ( $e_{\text{EB}} = 0.037 \pm 0.002$ ) orbit. The orbital plane of the EB is slightly inclined to the line of sight ( $i_{\text{EB}} = 87^\circ 33 \pm 0^\circ 06$ ), while that of the planet is inclined by  $\sim 2^\circ 5$  to the binary plane at the reference epoch. Orbital precession with a period of  $\sim 11$  yr causes the inclination of the latter to the sky plane to continuously change. As a result, the planet often fails to transit the primary star at inferior conjunction, causing stretches of hundreds of days with no transits (corresponding to multiple planetary orbital periods). We predict that the next transit will not occur until 2020. The orbital configuration of the system places the planet slightly closer to its host stars than the inner edge of the extended habitable zone. Additionally, the orbital configuration of the system is such that the CBP may experience Cassini State dynamics under the influence of the EB, in which the planet’s obliquity precesses with a rate comparable to its orbital precession. Depending on the angular precession frequency of the CBP, it could potentially undergo obliquity fluctuations of dozens of degrees (and complex seasonal cycles) on precession timescales.

**Key words:** binaries: eclipsing – planetary systems – stars: individual (KIC 12351927, Kepler-413) – techniques: photometric

*Online-only material:* color figures

### 1. INTRODUCTION

A mere 2 yr ago, Doyle et al. (2011) announced the discovery of the first transiting circumbinary planet (CBP), Kepler-16b. Six more transiting CBPs, including a multi-planet system, a CBP in the habitable zone, and a quadruple host stellar system, have been reported since (Welsh et al. 2012; Orosz et al. 2012a, 2012b; Kostov et al. 2013; Schwamb et al. 2013). In comparison, the number of planetary candidates orbiting single stars is significantly larger—3000 and counting (Burke et al. 2014).

Extensive theoretical efforts spanning more than two decades have argued that planets can form around binary stars (Alexander 2012; Paardekooper et al. 2012; Pierens & Nelson 2007, 2008a, 2008b, 2008c, 2013; Martin et al. 2013; Marzari et al. 2013; Meschiari 2012a, 2012b, 2013; Rafikov 2013). Simulations have shown that sub-Jupiter gas and ice giants should be common and, due to their formation and migration history, should be located near the edge of the circumbinary (CB) protoplanetary disk cavity. Indeed, that is where most of the CBPs discovered by *Kepler* reside! Once formed, it has been shown that CBPs can have dynamically stable orbits beyond

certain critical distance (Holman & Wiegert 1999). This distance depends on the binary mass fraction and eccentricity and is typically a few binary separations. All discovered CBP are indeed close to the critical limit—their orbits are only a few tens of percent longer than the critical separation necessary for stability (W. F. Welsh et al. 2014, in preparation). Additionally, models of terrestrial planet formation in close binary systems ( $a_{\text{bin}} < 0.4$  AU) indicate that accretion around eccentric binaries typically produces more diverse and less populated planetary systems compared with those around circular binaries (Quintana & Lissauer 2006). In contrast, the location of the ice line in CB protoplanetary disks is expected to be interior to the critical stability limit for 80% of wide, low-mass binary systems ( $M_{\text{bin}} < 4 M_\odot$ ) with  $a_{\text{bin}} \sim 1$  AU (Clanton 2013). Thus, Clanton argues, formation of rocky planets in such systems may be problematic. The theoretical framework of formation and evolution of planets in multiple stellar systems demands additional observational support, to which our latest CBP discovery Kepler-413 contributes an important new insight.

The configurations of six of the confirmed CBPs are such that they currently transit their parent stars every planetary orbit. Doyle et al. (2011) note, however, that the tertiary (planet transits across the primary star) of Kepler-16b will cease after 2018 and the quaternary (planet transits across the secondary

<sup>12</sup> NASA Earth and Space Science Graduate Fellow.

<sup>13</sup> Hubble Fellow.

star) will cease after 2014. The last transit of Kepler-35b was at BJD 2455965 (Welsh et al. 2012); it will start transiting again in a decade. As pointed out by Schneider (1994), some CBP orbits may be sufficiently misaligned with respect to their host eclipsing binary (EB) and hence precessing such that the above behavior may not be an exception. Additionally, Foucart & Lai (2013) argue that CB disks around sub-AU stellar binaries should be strongly aligned (mutual inclination  $\theta \leq 2^\circ$ ), in the absence of external perturbations by additional bodies (either during or after formation), whereas the disks and planets around wider binaries can potentially be misaligned ( $\theta \geq 5^\circ$ ). Foucart & Lai (2013) note that due to the turbulent environment of star formation, the rotational direction of the gas accreting onto the central protobinary is in general not in the same direction as that of the central core. Their calculations show that the CB disk is twisted and warped under the gravitational influence of the binary. These features introduce a back-reaction torque onto the binary, which, together with an additional torque from mass accretion, will likely align the CB protoplanetary disks and the host binary for close binaries but allow for misalignment in wider binaries.

The observational consequence of slightly misaligned CBPs is that they may often fail to transit their host stars, resulting in a light curve exhibiting one or more consecutive tertiary transits followed by prolonged periods of time where no transits occur. This effect can be further amplified if the size of the semimajor axis of the transited star projected upon the plane of the sky is large compared with the star's radius.

Such is the case of Kepler-413 (KIC 12351927), an 10.116146 day EB system. Its *Kepler* light curve exhibits a set of three planetary transits (separated by  $\sim 66$  days) followed by  $\sim 800$  days with no transits, followed by another group of five transits (again  $\sim 66$  days apart). We do not detect additional events  $\sim 66$  days (or integer multiples of) after the last transit. Our analysis shows that such peculiar behavior is indeed caused by a small misalignment and precession of the planetary orbit with respect to that of the binary star.

Here, we present our discovery and characterization of the CBP orbiting the EB Kepler-413. This paper is organized as an iterative set of steps that we followed for the complete description of the CB system. In Section 2, we describe our analysis of the *Kepler* data, followed by our observations in Section 3. We present our analysis and results in Section 4, discuss them in Section 5, and draw conclusions in Section 6.

## 2. KEPLER DATA

### 2.1. Kepler Light Curve

We extract the center times of the primary ( $T_p$ ) and secondary ( $T_o$ ) stellar eclipses, the normalized EB semimajor axes ( $a/R_A$ ), ( $a/R_B$ ), the ratio of the stellar radii ( $R_B/R_A$ ), and inclination ( $i_b$ ) of the binary and the flux contribution of star B from the *Kepler* light curve. Throughout this work, we refer to the primary star with a subscript “A”, to the secondary with a subscript “B”, and to the planet with a subscript “p”. We model the EB light curve of Kepler-413 with Eclipsing Light Curve (ELC) (Orosz et al. 2012a).

The *Kepler* data analysis pipeline (Jenkins et al. 2010a) uses a cosmic ray detection procedure that introduces artificial brightening near the middle of the stellar eclipses of Kepler-413 (see also Welsh et al. 2012). The procedure flags and corrects for positive and negative spikes in the light curves. The rapidly changing stellar brightness during the eclipse and

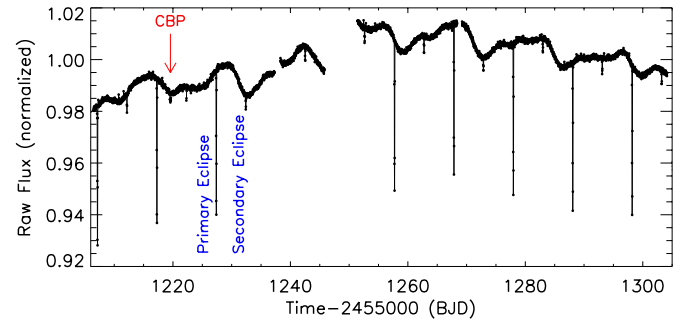


**Figure 1.** Section of the raw (SAPFLUX), normalized *Kepler* light curve of Kepler-413 spanning Quarter 15. The prominent stellar eclipses are clearly seen, with a depth of  $\sim 6\%$  and  $\sim 0.5\%$  for the primary and secondary eclipses, respectively. The last detected transit of the CBP is indicated with an arrow near day 1219. The gap near day 1250 is due to missing data.

(A color version of this figure is available in the online journal.)

the comparable width between the detrending window used by the pipeline and the duration of the stellar eclipse misleads the procedure into erroneously interpreting the mid-eclipse data points as negative spikes. This leads to the unnecessary application of the cosmic ray correction to the mid-eclipse data points prior to the extraction of the light curve. The target pixel files, however, contain a column that stores the fluxes, aperture positions, and times of each flagged cosmic ray event. To account for the anomalous cosmic ray rejection introduced by the pipeline, we add this column back to the flux column using fv (downloaded from the Kepler Guest Observer Web site) and then re-extract the corrected light curve using the *kepextract* package from PyKE (Still & Barclay 2012, Astrophysics Source Code Library, 8004)<sup>14</sup> (Kinemuchi et al. 2012). We note that our custom light curve extraction from the target pixel files for Quarters 1 through 14 introduces a known timing error of  $\sim 67$  s in the reported times that we account for.

Next, we detrend the normalized, raw *Kepler* data (SAPFLUX with a SAPQUALITY flag of 0) of Kepler-413 by an iterative fit with a high-order (50+) Legendre polynomial on a quarter-by-quarter basis. A representative section of the light curve, spanning Quarter 15, is shown in Figure 1. We use simple  $\sigma$ -clipping criteria, where points that are  $3\sigma$  above and below the fit are removed and the fit is recalculated. Next, the stellar eclipses are clipped out. We note that for our search for transiting CBPs, we do this for the entire EB catalog listed in Slawson et al. (2011) and B. Kirk et al. (2014, in preparation). The order of execution of the two steps (detrending and removal of stellar eclipses) generally depends on the baseline variability of the particular target. For quiet stars (like Kepler-413), we first remove the eclipses and then detrend.

Next, we phase fold the light curve of Kepler-413 on our best-fit binary star period of  $P = 10.116146$  days. For fitting purposes, we allow the limb-darkening coefficients of the primary star to vary freely. We note that star B is not completely occulted during the secondary stellar eclipse and its contribution to the total light during secondary eclipse needs to be taken into account. The best-fit models to the folded primary and secondary eclipses, based on the fast analytic mode of ELC (using Mandel & Agol 2002), are shown in Figure 2. The best-fit parameters for the ELC model of the *Kepler* light curve of Kepler-413 are listed in Table 1. Including a “third-light” contamination of 8% due to the nearby star (see V. B. Kostov et al. (2014,

<sup>14</sup> <http://keplerscience.arc.nasa.gov/PyKE.shtml>

**Table 1**  
Parameters of the Binary Star Systems

<b>Kepler-413</b>					
Parameter	Symbol	Value	Uncertainty ( $1\sigma$ )	Unit	Note
Orbital period	$P_{\text{bin}}$	10.116146	0.000001	day	<i>Kepler</i> photometry
Epoch of primary eclipse	$T_{\text{prim}}$	2454972.981520	...	BJD	Prša et al. (2011)
Epoch of secondary eclipse	$T_{\text{sec}}$	2454977.999	0.001	BJD	Prša et al. (2011)
Epoch of periastron passage	$T_0$	2454973.230	0.023	BJD	SOPHIE
Velocity semi-amplitude	$K_1$	43.489	0.085	$\text{km s}^{-1}$	SOPHIE
Velocity offset	$\gamma$	-27.78	0.05	$\text{km s}^{-1}$	SOPHIE
Argument of periapsis	$\omega_{\text{bin}}$	279.54 <sup>b</sup>	0.86	°	SOPHIE
Eccentricity	$e_{\text{bin}}$	0.0372	0.0017		SOPHIE
Orbital inclination	$i_{\text{bin}}$	87.3258	0.0987	°	<i>Kepler</i> photometry <sup>a</sup>
Normalized semimajor axis	$a_{\text{bin}}/R_A$	27.5438	0.0003		<i>Kepler</i> photometry <sup>a</sup>
Fractional radius	$R_B/R_A$	0.5832	0.0695		<i>Kepler</i> photometry <sup>a</sup>
Temperature of Star A	$T_A$	4700	...	K	Spectroscopic
Temperature ratio	$T_B/T_A$	0.7369	0.0153	K	<i>Kepler</i> photometry <sup>a</sup>
Limb-darkening Coeff. of Star A	$x_A$	0.3567	0.0615	K	<i>Kepler</i> photometry <sup>a</sup>
$V \sin i$ of Star A	$V \sin i$	5	2	$\text{km s}^{-1}$	SOPHIE
Fe/H of Star A	[Fe/H]	-0.2	...		NexSci <sup>c</sup>
Gravity of Star A	$\log(g)$	4.67	...		NexSci

#### Notes.

<sup>a</sup> ELC fit (Orosz et al. 2012a).

<sup>b</sup> Observer at  $-z$ .

<sup>c</sup> <http://exoplanetarchive.ipac.caltech.edu>.

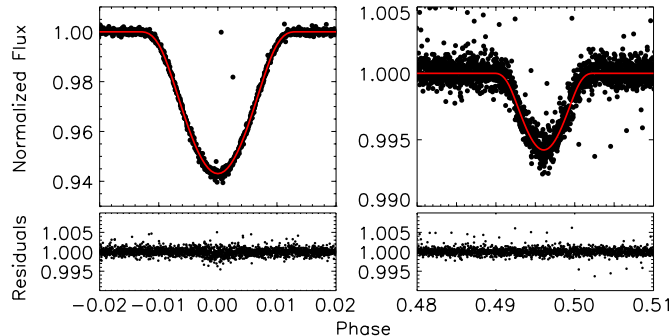


**Figure 2.** ELC model fits (solid lines) to the phase-folded primary (left) and secondary (right) stellar eclipses of Kepler-413 (black symbols); the lower panels show the best-fit residuals. The excess noise near the center of the transit is likely due to star spots.

(A color version of this figure is available in the online journal.)

in preparation), we obtain  $k = R_B/R_A = 0.5832 \pm 0.0695$ ,  $a/R_A = 27.5438 \pm 0.0003$ ,  $i_b = 87^\circ 3258 \pm 0^\circ 0987$ , and  $T_B/T_A = 0.7369 \pm 0.0153$ .

We measure the stellar eclipse times using the methodology of Orosz et al. (2012a). For completeness, we briefly describe it here. We extract the data around each eclipse and detrend the light curve. Starting with the ephemeris given by our best-fit model, we phase fold the light curve on the given period. Thus folded, the data were next used to create an eclipse template based on a cubic Hermite polynomial. Next, adjusting only the center time of the eclipse template, we iteratively fit it to each individual eclipse and measure the mid-eclipse times. To calculate eclipse time variations (ETVs), we fit a linear ephemeris to the measured primary and secondary eclipse times. The observed minus calculated (“ $O-C$ ”) residuals, shown in Figure 3, have rms amplitudes of  $A_{\text{prim}} \sim 0.57$  minute and  $A_{\text{sec}} \sim 8.6$  minutes, respectively. Primary eclipses near days (BJD−2,455,000) 63, 155, 185, 246, 276, 337, 559, 640, 802, 842, 903, 994, 1015, 1035, 1105, 1126, 1237, and 1247 have

been removed due to bad (with a flag of SAPQUALITY $\neq 0$ ) or missing data.  $A_{\text{sec}}$  is much larger than  $A_{\text{prim}}$  because the secondary eclipses are much shallower than the primary eclipses and therefore are much noisier.

The high precision of the measured primary ETVs allows us to constrain the mass of the CBP. The planet contributes to non-zero ETVs through the geometric light travel time and the dynamical perturbations it exerts on the EB (Borkovits et al. 2013). A CBP of  $10 M_{\text{Jup}}$  with the orbital configuration of Kepler-413 would cause primary ETVs with amplitudes of  $A_{\text{geometric}} \sim 1.2$  s and  $A_{\text{dynamic}} \sim 2.7$  minutes, respectively. The latter is  $\sim 3\sigma$  larger than the measured amplitude of the primary ETVs, indicating an upper limit for the mass of the CBP of  $\sim 10 M_{\text{Jup}}$  and thereby confirming its planetary nature.

## 2.2. Discovering the Transits of Kepler-413b

We discovered the planetary transits of Kepler-413b using the method described in Kostov et al. (2013). For completeness, we briefly outline it here.

Due to the aperiodic nature of the transits of a CBP, traditional methods used to search for periodic signals are not adequate. The amplitude of the transit timing variations between consecutive transits of Kepler-413b, for example, are up to two days ( $\sim 3\%$  of one orbital period), compared with an average transit duration of fewer than 0.5 days. To account for this, we developed an algorithm tailored for finding individual box-shaped features in a light curve (Kostov et al. 2013), based on the widely used Box-fitting Least Squares (BLS) method (Kovács et al. 2002). To distinguish between systematic effects and genuine transits, we incorporated the methodology of Burke et al. (2006).

Our procedure is as follows. Each detrended light curve is segmented into smaller sections of equal lengths (dependent on the period of the EB and on the quality of the detrending). Next, each section is replicated  $N$  times (the number is arbitrary) to create a periodic photometric time series. We apply BLS to each and search for the most significant positive (transit) and negative (anti-transit, in the inverted time-series flux)

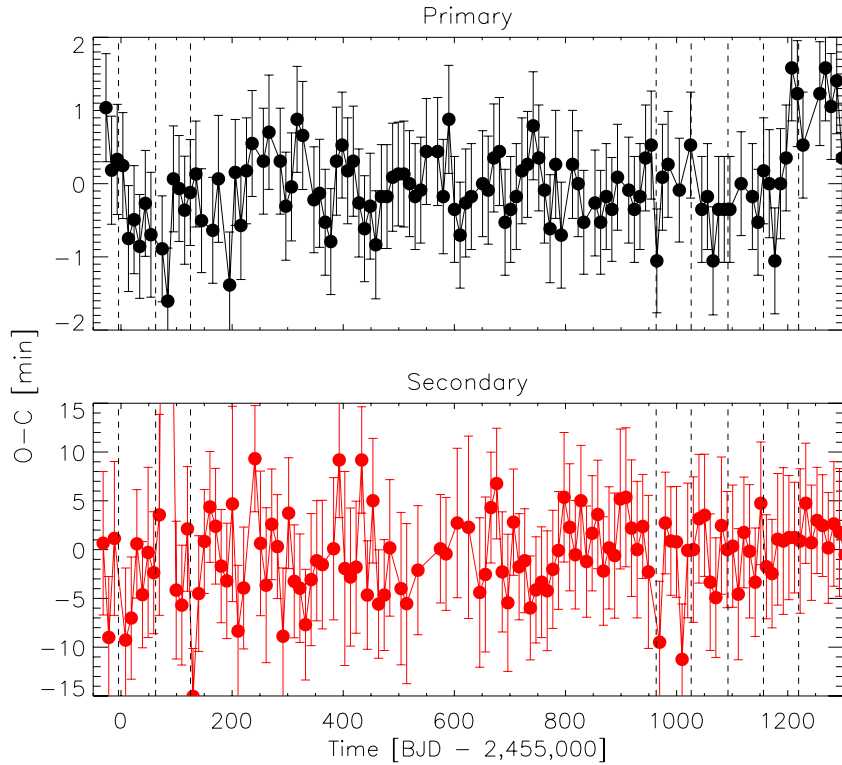


**Figure 3.** ETVs of the primary (upper panel, black) and secondary (lower panel, red online gray in the printed journal) eclipses of Kepler-413, in terms of observed vs. calculated (“ $O-C$ ”) deviations from the linear ephemeris in minutes. The vertical dashed lines indicate the times of the planetary transits. The “ $O-C$ ” deviations are consistent with noise; there are no discernible trends or periodicities. The last eight points of the primary ETVs are excluded from our ETV analysis, as their anomalous shift by  $\sim 1$  minute after day BJD 1200 is caused by a known ([http://archive.stsci.edu/kepler/release\\_notes/release21/DataRelease\\_21\\_20130508.pdf](http://archive.stsci.edu/kepler/release_notes/release21/DataRelease_21_20130508.pdf)) absolute timing error of  $\sim 67$  s for target pixel files from Quarters 1 through 14.

(A color version of this figure is available in the online journal.)

box-shaped features. We compare the goodness of fit of the two in terms of the  $\Delta\chi^2$  difference between the box-shaped model and a straight line model. Systematic effects (positive or negative) present in a particular segment will have similar values for  $\Delta(\chi^2)_{\text{transit}}$  and  $\Delta(\chi^2)_{\text{anti-transit}}$ . On the contrary, a segment with a dominant transit (or anti-transit) feature will be clearly separated from the rest in a  $\Delta(\chi^2)_{\text{transit}}$  versus  $\Delta(\chi^2)_{\text{anti-transit}}$  diagram.

The (transit)–(anti-transit) diagram for Kepler-413 is shown in Figure 4. The segments of the light curve where no preferable signal (transit or anti-transit) is detected form a well-defined cloud, symmetrically distributed along the  $(\Delta(\chi^2)_{\text{transit}})/(\Delta(\chi^2)_{\text{anti-transit}}) = 1$  line. The segments containing the transits of the CBP marked in red (or gray) diamonds, along with a few other segments where systematic features dominate (black circles), exhibit a preferred  $\Delta(\chi^2)_{\text{transit}}$  signal. The blue line represents the merit criterion adopted for this target, defined in terms of an iteratively chosen ratio of  $(\Delta(\chi^2)_{\text{transit}})/(\Delta(\chi^2)_{\text{anti-transit}}) = 2$ .

The signal for all but one (transit 7) of the Kepler-413b transits is very strong. That transit 7 falls short of the criterion is not surprising. This event is the shortest and also the shallowest and can be easily missed even when scrutinized by eye. For Kepler-413, we had a preliminary dynamical model of the system based on events 1 through 6, prior to the release of Quarter 14 data. The observed events 7 and 8 were very near the predicted times, providing additional constraints on our model.

### 2.3. Stellar Rotation

Flux modulations of up to  $\sim 1\%$  on a timescale of  $\sim 13$  days are apparent in the light curve of Kepler-413. We assume that

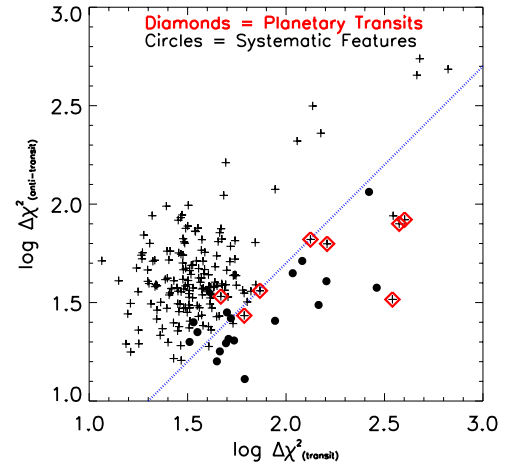


**Figure 4.** (Transit)–(anti-transit) diagram for Kepler-413. Each symbol represents the logarithmic ratio between the best transit and anti-transit signals detected in individual segments. The planetary transits are marked as red (gray in the printed journal) diamonds and the merit criterion line is marked in blue. Black circles indicate segments where known systematic features mimic transits. (A color version of this figure is available in the online journal.)

the source of this variation is star spots carried along with the rotation of the stellar surface of the primary, the dominant flux contributor ( $\sim 85\%$ ) in the *Kepler* bandpass. To calculate the rotation period of star A, we compute Lomb–Scargle (L-S) periodograms and perform wavelet analysis (using a Morlet wavelet of order 6; Torrence & Compo 1998) for each quarter separately. No single period matches all quarters because of spot

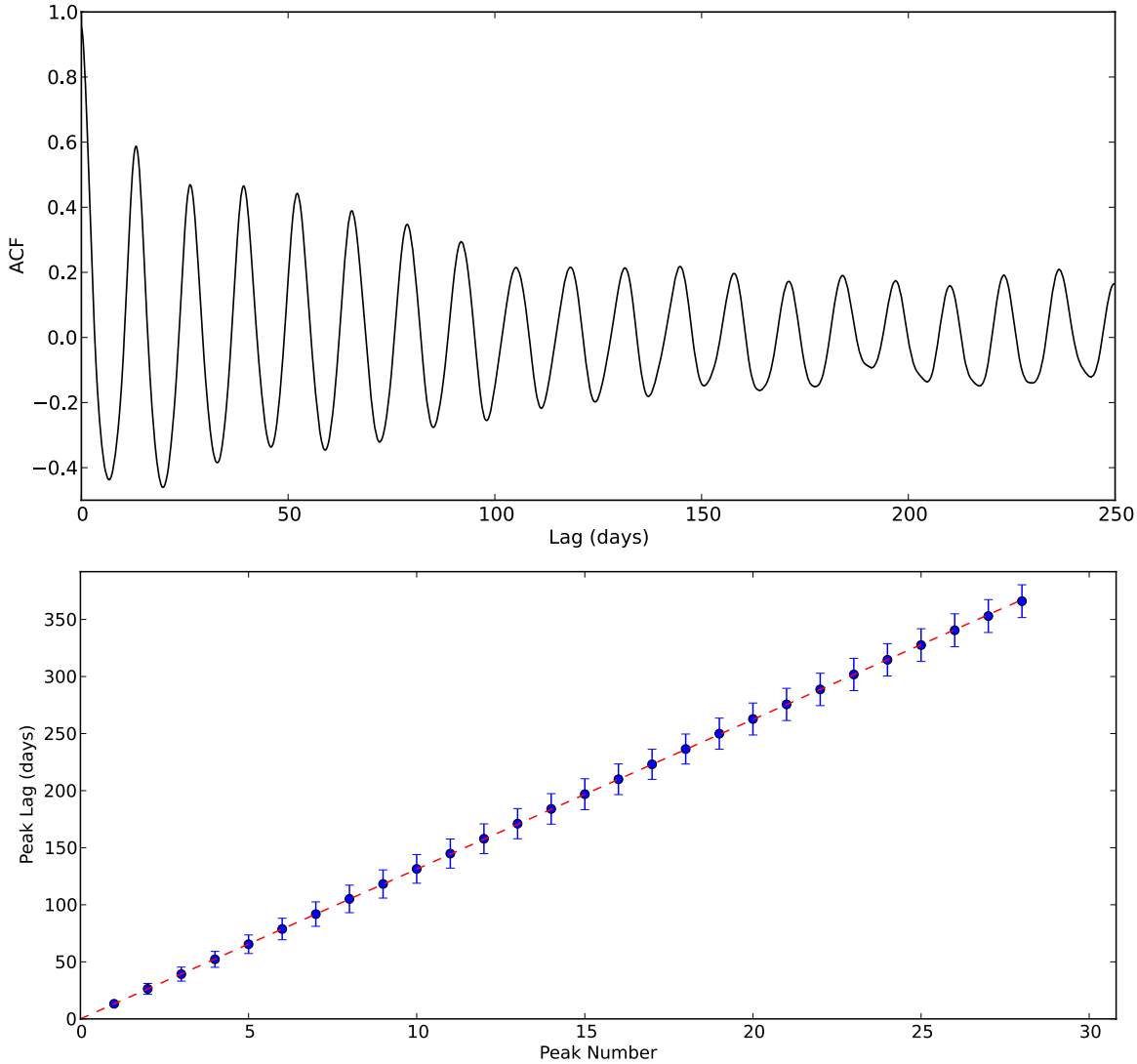


**Figure 5.** Upper panel: the ACF of the cleaned and detrended light curve after the removal of the stellar eclipses (solid symbols), fit with a straight line (dashed line).

(A color version of this figure is available in the online journal.)

evolution as spots emerge/disappear (the most dramatic change, for example, being during Quarter 10). We estimate an average rotation period across all quarters of  $P_{\text{rot},A} = 13.1 \pm 0.3$  days and  $P_{\text{rot},A} = 12.9 \pm 0.4$  days from L-S and wavelet analysis, respectively.

In addition, we measured the degree of self-similarity of the light curve over a range of different time lags by performing an autocorrelation function (ACF) analysis. In the case of rotational modulation, repeated spot-crossing signatures produce ACF peaks at lags corresponding to the rotation period and its integer multiples (McQuillan et al. 2013a). Figure 5 depicts the ACF of the cleaned and detrended light curve, after the primary and secondary eclipses were removed and replaced by the value of the mean light curve with a typical random noise. The autocorrelation reveals clear stable modulation with a period of about 13 days. To obtain a more precise value of the stellar rotation, we measured the lags of the first 25 peaks of the autocorrelation and fit them with a straight line, as shown in the lower panel of Figure 5 (McQuillan et al. 2013b). From the slope of the fitted line, we derived a value of  $P_{\text{rot},A} = 13.15 \pm 0.15$  days

as our best value for the stellar rotation period, consistent with the rotation period derived from the L-S analysis.

We carefully inspected the light curve to verify the period and to ensure that it did not correspond to any harmonic of the spin period. A 13.1 day period matches the spot modulation well. Using the stellar rotation velocity measured from our spectral analysis, we derive an upper limit to star A's radius of  $R_A \leq 1.29 R_\odot$ . The surface gravity of star A,  $\log g_A = 4.67$ , provided by the NASA Exoplanet Archive<sup>15</sup>, in combination with the upper limit on  $R_A$ , indicates  $M_A \leq 2.82 M_\odot$ .

#### 2.4. Doppler Beaming

A radiation source emitting isotropically and moving at nonrelativistic speed with respect to the observer is subject to a Doppler beaming effect (Rybicki & Lightman 1979). The apparent brightness of the source increases or decreases as it respectively moves toward or away from the observer. To calculate the Doppler beaming factor for star A, we approximate its spectrum as that of a blackbody with  $T_{\text{eff}} = 4700$  K

<sup>15</sup> <http://exoplanetarchive.ipac.caltech.edu>

(see the next section) and the *Kepler* data as monochromatic observations centered at  $\lambda = 600$  nm. Using Equations (2) and (3) from Loeb & Gaudi (2003), we estimate the boost factor  $3 - \alpha = 5.13$ . For the value of  $K_1 = 43.49$  km s $^{-1}$  derived from the radial velocity (RV), we expect a Doppler beaming effect due to star A with an amplitude of  $\sim 750$  ppm, on par with the intrinsic rms of the individual *Kepler* measurements. The Doppler beaming contribution due to star B is much smaller (amplitude of  $\sim 50$  ppm) because of its small contribution to the total brightness of the system.

To search for the signal due to star A, we do a custom data detrending of the *Kepler* light curve tailored to the rotational modulations. To each data point  $t_i$ , we fit either one or more sine waves with the same mean and period (but different phases and amplitudes) centered on the  $[-0.5P_{\text{rot},A} + t_i, t_i + 0.5P_{\text{rot},A}]$  interval. The mean values of the best-fit sine waves at each point represent a rotation-free light curve. Few sections of the light curve are consistent with a single spot (or group of spots) rotating in and out of view and can be modeled with one sinusoid; most need two or more. The continuously evolving spot pattern, the faintness of the source, and the fact that the binary period is close to the rotation period of the primary star make detection of the otherwise strong expected signal ( $\sim 750$  ppm) challenging. Despite the custom detrending, the modulations in the processed data are consistent with noise and we could not detect the Doppler beaming oscillations caused by the motion of star A. We note that we successfully detected the Doppler beaming effect for Kepler-64 (Kostov et al. 2013), where the amplitude is smaller but the target is brighter and the rms scatter per 30 minute cadence is smaller.

### 3. FOLLOW-UP OBSERVATIONS

#### 3.1. SOPHIE

Kepler-413 was observed 2012 September–October and 2013 March–April with the SOPHIE spectrograph at the 1.93 m telescope of Haute-Provence Observatory, France. The goal was to detect the reflex motion of the primary star due to its secondary component through RV variations. SOPHIE (Bouchy et al. 2009) is a fiber-fed, cross-dispersed, environmentally stabilized échelle spectrograph dedicated to high-precision RV measurements. The data were secured in high-efficiency mode (resolution power  $R = 40,000$ ) and slow read-out mode of the detector. The exposure times ranged between 1200 and 1800 s, allowing for a signal-to-noise ratio per pixel in the range 4–8 to be reached at 550 nm. The particularly low signal-to-noise ratio is due to the faintness of the target ( $K_p = 15.52$  mag).

The spectra were extracted from the detector images with the SOPHIE pipeline, which includes localization of the spectral orders on the two-dimensional images, optimal order extraction, cosmic ray rejection, wavelength calibration, and corrections for the flat field. Then, we performed a cross correlation of the extracted spectra with a G2-type numerical mask including more than 3500 lines. Significant cross-correlation functions (CCFs) were detected despite the low signal-to-noise ratio. Their Gaussian fits allow RVs to be measured, as well as associated uncertainties, following the method described by Baranne et al. (1996) and Pepe et al. (2002). The FWHM of those Gaussians is  $11 \pm 1$  km s $^{-1}$  and the contrast is  $12\% \pm 4\%$  of the continuum. One of the observations (BJD = 2,456,195.40345) was corrected from the  $230 \pm 30$  m s $^{-1}$  blueshift due to Moon light pollution and measured thanks to the reference fiber pointed on the sky (e.g., Hébrard et al. 2008). The other

**Table 2**  
Measured RVs

BJD <sub>UTC</sub> −2,400,000	RV (km s $^{-1}$ )	$\pm 1\sigma$ (km s $^{-1}$ )
56 180.42595	−59.89	0.20
56 184.39404	15.59	0.19
56 186.44561	−14.52	0.09
56 187.47375	−43.73	0.10
56 192.42495	−16.21	0.16
56 195.40345 <sup>a</sup>	9.99	0.25
56 213.36121	−0.37	0.17
56 362.67907	−56.59	0.16
56 401.55880	−71.26	0.14
56 403.56461	−47.72	0.27
56 404.62680	−21.87	0.19

Note. <sup>a</sup> Measurement corrected for sky background pollution.

exposures were not significantly polluted by sky background or by light from the Moon. The measured RVs are reported in Table 2 and plotted in Figure 6. RVs show significant variations in phase with the *Kepler* ephemeris.

The RVs were fit with a Keplerian model, taking into account the three constraints derived from the *Kepler* photometry: the orbital period  $P$  and the mid-times of the primary and secondary stellar eclipses,  $T_{\text{prim}}$  and  $T_{\text{sec}}$ , respectively. The fits were made using the PASTIS code (Díaz et al. 2013), previously used by, e.g., Santerne et al. (2011); Hébrard et al. (2013). Confidence intervals around the best solutions were determined by Monte Carlo simulations. The histograms of the obtained parameters have a single peak. We fitted them with Gaussians, whose centers and widths are the derived values and uncertainties reported in Table 1. The best fits are overplotted with the data in Figure 6. The dispersion of the residuals of the fit is 106 m s $^{-1}$ , in agreement with the error bars of the RV measurements. We did not detect any significant drift of the RVs in addition to the reflex motion due to the binary. The small difference between the stellar eclipses,  $T_{\text{prim}} - T_{\text{sec}}$ , and  $P/2$  measured from *Kepler* photometry indicates that the orbit is not circular. Together with the RVs, it allows for the detection of a small but significant eccentricity  $e = 0.037 \pm 0.002$  and longitude of the periastron  $\omega = 279.54 \pm 0.86$ . We note that our spectroscopic observations determined Kepler-413 to be a single-lined spectroscopic binary and allowed us to evaluate the binary mass function  $f(m)$  from the derived RV semi-amplitude of the primary star  $K_1 = 43.485 \pm 0.085$  km s $^{-1}$ .

The signal-to-noise ratio of the final co-added spectrum is too low to allow for a good spectral analysis of the star. The profile of the H $\alpha$  line suggests an effective temperature  $T_{\text{eff}} \simeq 4700$  K. The width of the CCF implies  $v \sin i_* = 5 \pm 2$  km s $^{-1}$ .

#### 3.2. Third-light Companion

The large *Kepler* pixels,  $4'' \times 4''$  (Jenkins et al. 2010b), are prone to photometric contamination due to background sources. Unaccounted extra light inside the target’s aperture can contribute to an erroneous interpretation of eclipse and transit depths, resulting in incorrect estimation of the relative sizes of the occulting objects. Proper characterization of such contamination is particularly important for the analysis of CBPs (e.g., Schwamb et al. 2013; Kostov et al. 2013).

We note that there is a visible companion (“third light”) inside the central pixel of Kepler-413 at a separation of  $\sim 1''.6$  from the target, with a magnitude difference of  $\Delta K_p \sim 2.8$  (V. B. Kostov et al. 2014, in preparation). The presence of the companion

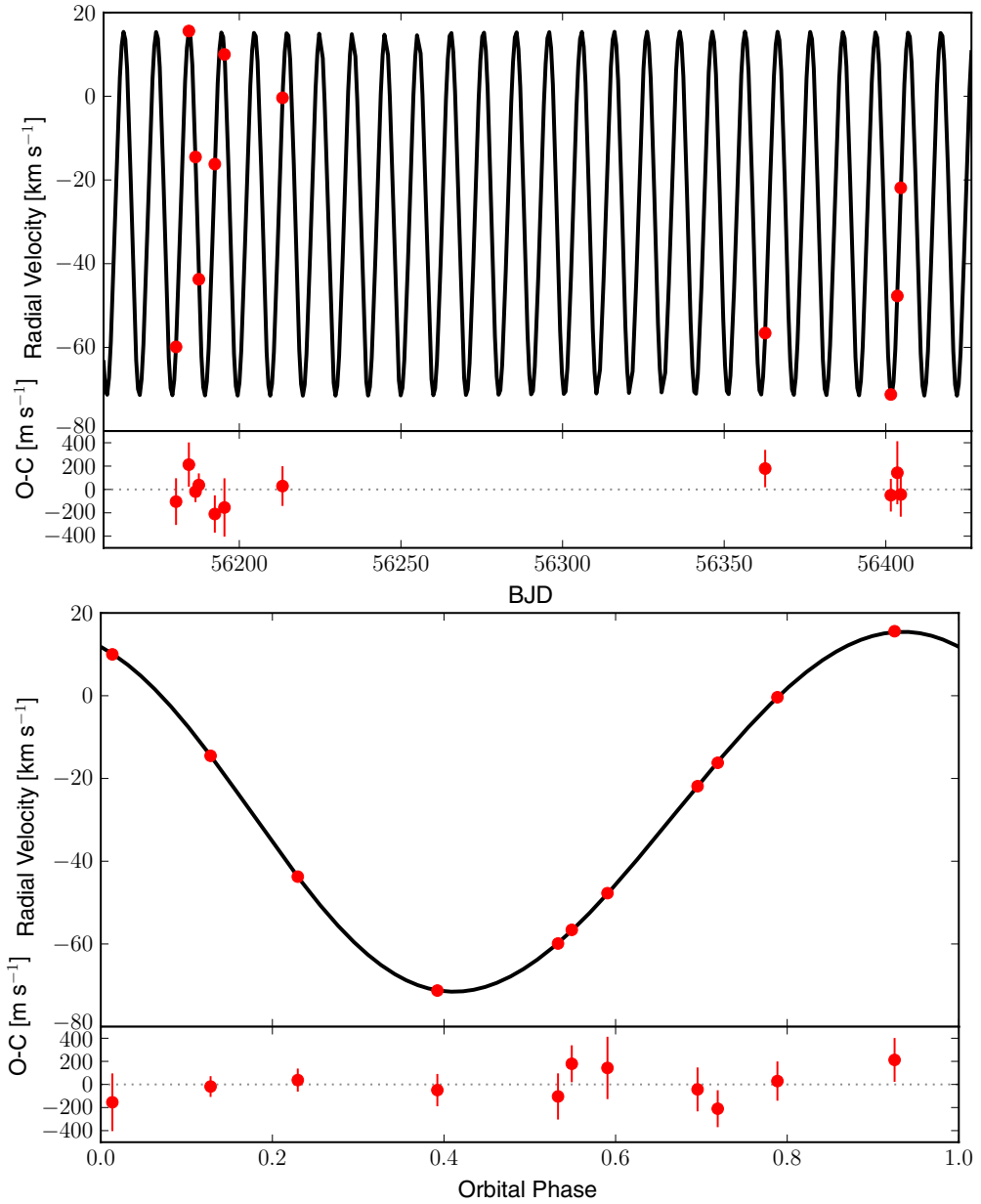


**Figure 6.** SOPHIE RV measurements of Kepler-413 with  $1\sigma$  error bars as a function of time (upper) or orbital phase (lower), together with their Keplerian fit and residuals of the fit. Note the scale is km s<sup>-1</sup> for the RVs and m s<sup>-1</sup> for the O-C residuals.

(A color version of this figure is available in the online journal.)

can be deduced from Two Micron All Sky Survey (2MASS; Skrutskie et al. 2006) and UKIRT (Lawrence et al. 2007) images and from the full frame *Kepler* image. A marked asymmetry in the target's point spread function, exhibited as a side bump with a position angle of  $\sim 218^\circ$ , hints at the presence of an object close to Kepler-413.

During our reconnaissance spectroscopy with the 3.5 m Apache Point Observatory telescope, we noticed the companion as a clearly separated star  $\sim 1.^{\circ}6$  away from Kepler-413. The companion was physically resolved using adaptive optics-assisted photometry from Robo-AO (Baranec et al. 2013) and seeing-limited infrared photometry from WIYN/WHIRC (Meixner et al. 2010). The measured flux contribution from the companion to the aperture of Kepler-413 is  $\sim 8\%$ ,  $\sim 15\%$ ,  $\sim 19\%$ , and  $\sim 21\%$  in the *Kepler*, *J*, *H*, and *K<sub>s</sub>* bands, respectively (V. B. Kostov et al. 2014, in preparation);

we correct for the contamination in our analysis. A detailed discussion of the companion's properties will be presented in future work (V. B. Kostov et al. 2014, in preparation).

The presence of such contamination is not unusual: adaptive optics observations of 90 *Kepler* planetary candidates show that  $\sim 20\%$  of them have one visual companion within  $2''$  (Adams et al. 2012); lucky imaging observations by Lillo-Box et al. (2012) find that  $\sim 17\%$  of 98 *Kepler* Objects of Interest have at least one visual companion within  $3''$ . As more than 40% of spectroscopic binaries with  $P < 10$  days are member of triple systems according to Tokovinin et al. (2006), it is reasonable to consider the visible companion to be gravitationally bound to Kepler-413. Using Table 3 of Gilliland et al. (2011), for a contaminating star of  $K_p \leqslant 18.5$  mag (i.e.,  $\Delta K_p \leqslant 3$  mag), and interpolating for the Galactic latitude of Kepler-413 of  $b = 17^\circ 47'$ , we estimate the probability of a random alignment

between a background source and Kepler-413 within an area of radius  $1''.6$  to be  $\sim 0.002$ . That despite the odds there is a star within this area indicates that the “third light” source is gravitationally bound to the EB and could provide a natural mechanism for the observed misalignment of Kepler-413b. Based on this statistical estimate, we argue that Kepler-413b is a CBP in a triple stellar system.

#### 4. ANALYSIS OF THE SYSTEM

A complete description of a CBP system requires 18 parameters—three masses ( $M_A$ ,  $M_B$ , and  $M_p$ ), three radii ( $R_A$ ,  $R_B$ , and  $R_p$ ), six orbital elements for the binary system ( $a_{\text{bin}}$ ,  $e_{\text{bin}}$ ,  $\omega_{\text{bin}}$ ,  $i_{\text{bin}}$ ,  $\Omega_{\text{bin}}$ , and phase  $\phi_{0,\text{bin}}$ ), and six osculating orbital elements for the CBP ( $a_p$ ,  $e_p$ ,  $\omega_p$ ,  $i_p$ ,  $\Omega_p$ , and  $\phi_{0,p}$ ). As described in Sections 2 and 3, some of these parameters can be evaluated from either the *Kepler* data or from follow-up photometric and spectroscopic observations. Measurements of the stellar RVs provide  $e_{\text{bin}}$ ,  $\omega_{\text{bin}}$ ,  $i_{\text{bin}}$ , and the binary mass function  $f(m)$  (but not the individual stellar masses, as we observed Kepler-413 as a single-lined spectroscopic binary). The relative sizes of the two stars and the inclination of the binary system are derived from the *Kepler* light curve. Based on the measured ETVs, we approximate the planet as a test particle ( $M_p = 0$ ) for our preliminary solution of the system and solve for its mass with the comprehensive photodynamical model. The value of  $\Omega_{\text{bin}}$  is undetermined (see Doyle et al. 2011; Welsh et al. 2012), unimportant to our analysis, and is set equal to zero.

Here, we derive the mass of the EB (thus the masses of the primary and secondary stars) and the radius of the primary star from the planetary transits. Next, we produce a preliminary numerical solution of the system—a necessary input for the comprehensive photometric dynamical analysis we present in Section 4.2. We study the dynamical stability of Kepler-413b in Section 4.3.

##### 4.1. Initial Approach: Planetary Transits and Preliminary Solutions

The mid-transit times, durations, and depths of consecutive transits of a CBP are neither constant nor easy to predict when the number of observed events is low. However, while strictly periodic transit signals can be mimicked by a background contamination (either an EB or a planet), the variable behavior of CBP transits provides a unique signature without common false positives.

Different outcomes can be observed depending on the phase of the binary system. While the CBP travels in one direction on the celestial sphere when at inferior conjunction, the projected velocities of each of the two stars can be in either direction. When the star and the planet move in the same direction, the duration of the transit will be longer than when the star is moving in the opposite direction with respect to the planet. As shown by Kostov et al. (2013), the transit durations as a function of binary phase can be used to constrain the a priori unknown mass of the binary and the radius of the primary star (both critical parameters for the photodynamical model described below), assuming that the planet transits across the same chord on the star. Typically, the more transits observed and the wider their EB phase coverage, the tighter the constraints are.

While useful for favorable conditions, the approximation of Kostov et al. (2013) is not applicable in general and we extend it here. Depending on the relative positions of the CBP and the star on the sky, the CBP will transit across different chord

lengths with associated impact parameters, such that different transits will have different durations and depths. A particular situation may be favorable, such as the cases of Kepler-64b and Kepler-47b, where the CBPs transit across approximately constant chords. While the chords lengths do change from one transit to another, the variations are small as the stellar radii are sufficiently large, the mutual inclination between the orbits of the CBP and the EB is small, and the approximation in Kostov et al. (2013) applies. The situation for Kepler-413, however, is quite the opposite—due to the misalignment between the two orbits and the small stellar radius, the chord length changes so much from one transit to another that the impact parameter is often larger than  $R_A + R_p$ , i.e., the planet misses a transit. To properly account for this novel behavior of a CBP, we modify our analytic approach accordingly to allow for variable impact parameter. Expanding on Equation (4) of Kostov et al. (2013), we add another term ( $D$ ) to the numerator:

$$t_{\text{dur},i} = \frac{ABD_i}{1 + ACx_i}, \quad (1)$$

$$\begin{aligned} A &= (M_{\text{bin}})^{-1/3} \\ B &= 2R_c \left( \frac{P_p}{2\pi G} \right)^{1/3} \\ C &= -f(m)^{1/3} \left( \frac{P_p}{P_{\text{bin}}} \right)^{1/3} (1 - e^2)^{-1/2} \\ D_i &= \sqrt{1 - b_i^2} \\ x_i &= (e \sin \omega + \sin(\theta_i + \omega)), \end{aligned} \quad (2)$$

where  $t_{\text{dur},i}$ ,  $b_i$ , and  $\theta_i$  are the duration, impact parameter, and binary phase of the  $i$ th transit, respectively,  $M_{\text{bin}}$  is the sum of the masses of the two stars of the EB,  $P_p$  is the average period of the CBP,  $R_c = R_A + R_p$  is the transited chord length (where  $R_A$  and  $R_p$  are the radius of the primary star and the planet, respectively),  $f(m)$  is the binary mass function (Equation (2.53), Hilditch 2001), and  $e$  and  $\omega$  are the binary eccentricity and argument of periastron, respectively. Applying Equation (1) to transits with  $b > 0$  results in smaller derived  $M_{\text{bin}}$  compared with transits across a maximum chord,  $b = 0$ .

The generally used method to derive  $b$  from the measured transit durations and depths for a planet orbiting a single star (Seager & Mallén-Ornelas 2003) is not applicable for a CBP. The CBP impact parameter cannot be easily derived from the observables. From geometric considerations,  $b$  is

$$b = \sqrt{(x_s - x_p)^2 + (y_s - y_p)^2}, \quad (3)$$

where  $(x_s, y_s)$  and  $(x_p, y_p)$  are the sky  $x$ - and  $y$ -coordinates of the star and the planet, respectively. The former depend on the binary parameters only and can be calculated from Hilditch (2001):<sup>16</sup>

$$\begin{aligned} x_s &= r_s \cos(\theta_{\text{bin}} + \omega_{\text{bin}}) \\ y_s &= r_s \sin(\theta_{\text{bin}} + \omega_{\text{bin}}) \cos i_{\text{bin}}, \end{aligned} \quad (4)$$

where  $r_s$ ,  $\omega_{\text{bin}}$ ,  $\theta_{\text{bin}}$ , and  $i_{\text{bin}}$  can be directly estimated from the RV measurements and from the *Kepler* light curve. The CBP coordinates, however, depend on the unknown mass of the

<sup>16</sup> Generally,  $\Omega_{\text{bin}}$  (the EB longitude of the ascending node) is undetermined and assumed to be zero.

binary and on the instantaneous orbital elements of the CBP  $\Omega_p$ ,  $\theta_p$ , and  $i_p$ . Assuming a circular orbit for the CBP:

$$\begin{aligned} x_p &= a_p[\cos(\Omega_p)\cos(\theta_p) - \sin(\Omega_p)\sin(\theta_p)\cos(i_p)] \\ y_p &= a_p[\sin(\Omega_p)\cos(\theta_p) + \cos(\Omega_p)\sin(\theta_p)\cos(i_p)], \end{aligned} \quad (5)$$

where  $a_p$  is the semimajor axis of the CBP. For a misaligned CBP like Kepler-413b, however,  $\Omega_p \neq 0.0$  and Equation (5) cannot be simplified any further. In addition, due to three-body dynamics, all three CBP orbital parameters vary with time. As a result, incorporating Equation (3) into Equation (1) will significantly complicate the solution.

However, we note that Equation (1) uses only part of the information contained in the *Kepler* light curve, i.e., transit durations and centers; it does not capitalize on the depth or shape of each transit. To fully exploit the available data, we evaluate the impact parameters of the eight transits directly from the light curve by fitting a limb-darkened transit model Mandel & Agol (2002) to each transit individually. The procedure is as follows. First, we scale the CB system to a reference frame of a mock, stationary primary star with a mass equal to the total binary mass of Kepler-413. The scaling is done by adjusting for the relative velocities of the primary star Kepler-413 A ( $V_{x,A}$ ) and the CBP ( $V_{x,p}$ ). The impact parameters are not modified by the scaling, as it does not change the distance between the planet and the star or their mutual inclination during each transit. We approximate  $V_{x,p}$  as a single value for all transits:

$$V_{x,p} = \left( \frac{2\pi GM_{\text{bin}}}{P_p} \right)^{1/3} = \text{const.} \quad (6)$$

A mock planet orbits the star on a circular,  $P_p = 66$  day orbit (the period of Kepler-413b). The relative velocity of the observed CBP at the time of each transit ( $V_{x,\text{obs},i}$ ) is calculated as the absolute difference between the instantaneous  $V_{x,p}$  and  $V_{x,A}$ :

$$V_{x,\text{obs},i} = |V_{x,p} - V_{x,A,i}|, \quad (7)$$

where  $V_{x,A,i}$  can be calculated from the fit to the RV measurements. The scaled time of the  $i$ th mock transit  $t_{\text{mock},i}$ , referred to as the time of minimum light, is then

$$t_{\text{mock},i} = \frac{|V_{x,p} - V_{x,A,i}|}{V_{x,p}} t_{\text{obs},i}, \quad (8)$$

where  $t_{\text{obs},i}$  is the observed time during the  $i$ th transit. The mock transits are “stretched” with respect to the observed ones when  $V_{x,A} < 0$  and “compressed” when  $V_{x,A} > 0$ .

While  $V_{x,p}$  depends on the unknown binary mass, it does so by only its third root (Equation (6)). For the low-mass binary we expect from the *Kepler* Input Catalog,  $V_{x,p}$  varies only by  $\sim 26\%$  for  $M_{\text{bin}}$  between  $1.0 M_{\odot}$  and  $2.0 M_{\odot}$ . Thus, the dominant factor in Equation (8) is  $V_{x,A,i}$ .

The eight scaled, mock transits are next fit individually, sharing the same binary mass  $M_{\text{bin}}$ , size of the primary star  $R_A$ , and the CBP radius  $R_p$ . The normalized semimajor axis of the mock planet,  $a_{\text{mock}}/R_A$ , depends on the binary phase of each transit and is different for different transits—for fitting purposes, it ranges from  $(a_p - a_A)/R_A$  for transits near secondary stellar eclipse to  $(a_p + a_A)/R_A$  for those near primary eclipse. Here,  $a_p$  is the mean semimajor axis of the CBP Kepler-413b and  $a_A$  is the semimajor axis of the primary star Kepler-413-A. For light curve modeling, we use the limb-darkening coefficients from Section 2.

To estimate  $R_p/R_A$ , we first fit a limb-darkened light-curve model to the scaled transit 8. The binary star is near a quadrature during the transit,  $|V_{x,A,i}|$  is near zero,  $a_{\text{mock}} \approx a_p$ ,  $M_{\text{bin}}$  does not significantly affect Equation (8), and the scaling is minimal ( $t_{\text{mock},i} \approx t_{\text{obs},i}$ ). To confirm that the scaling is negligible, we fit transit 8 for all  $M_{\text{bin}}$  between 1.0 and 2.0. The differences between the derived values for  $R_{p,8}/R_A$  are indistinguishable— $R_{p,8}/R_A = 0.053$  for all  $M_{\text{bin}}$ , where  $R_{p,8}$  is the radius of the planet deduced from the fit to scaled transit 8. We next use  $R_{p,8}$  for light-curve fitting of the other seven scaled transits. Also, the best-fit  $a_{\text{mock},8}$  from transit 8 is used in combination with  $a_A$  to constrain the allowed range for  $a_{\text{mock},1-7}$  for the other seven transits, as described above. We note that while transit 1 also occurs near quadrature, the transit duration and depth are both much smaller than those of transit 8, making the latter a better scaling ruler. The derived impact parameters for transits 1 through 8 are 0.85, 0.71, 0.17, 0.61, 0.84, 0.67, 0.78, and 0.05, respectively. We note that these are used to estimate  $M_{\text{bin}}$  in Equation (1) only and not as exact inputs to the photodynamical analysis described below.

To evaluate the applicability of our approach, we test it on synthetic light curves designed to mimic Kepler-413b (8 transits, 10–11 misses, CBP on a  $\sim 66$  day orbit). For a noiseless light curve, we recover the simulated impact parameters of the 8 transits to within 0.01, the semimajor axis to within 1%, and the size of the planet to within 10%. Allowing the (known) mass of the simulated binary star to vary by  $\pm 0.5 M_{\odot}$  modifies the derived impact parameters by no more than 0.02. For a simulated set of light curves with normally distributed random noise of  $\sim 700$  ppm rms per 30 minute cadence (similar to that of Kepler-413), we recover the impact parameters to within 0.15 and the semimajor axis and the size of the planet each to within 10%. The good agreement between the derived and simulated model values validates the method. The observed (black) and scaled (green or light color) transits of Kepler-413b and the best-fit models (red or gray) to the latter are shown in Figure 7.

We note that there are secondary effects not taken into account by Equation (8).  $V_{x,A}$ , assumed to be constant in the equation, in reality varies throughout the duration of the transit. In principle, the longer the CBP transit, the more the stellar velocity and acceleration deviate from constancy. Longer transits (like transit 6; see Figure 7) have asymmetric shapes and the circular orbit approximation for the CBP in Equation (8) is not optimal. Depending on the phase of the binary star at the time of transit, both the magnitude and the sign of  $V_{x,A}$  may change—near quadrature, for example, the star changes direction.

Next, we apply Equation (1) to the eight transits of Kepler-413b for constant and variable chords and compare the results. The best-fit models for the two cases are shown in Figure 8 as the blue and red curve, respectively. The derived values for  $M_{\text{bin}}$  and  $R_A$  are 1.41 and 0.70 for constant  $b$  and 1.33 and 0.91 for varying  $b$ . Not accounting for different impact parameters overestimates  $M_{\text{bin}}$  and underestimates  $R_A$ .

We use the measured transit duration uncertainties to constrain the derived binary mass, as follows. We simulate a set of 10,000 scrambled observations, each consisting of the eight measured transit durations individually perturbed by adding normally distributed noise with a standard deviation of 20 minutes. Next, we apply Equation (1) to each realization. The distribution of the derived  $M_{\text{bin}}$  for the entire set of scrambled observation is shown in Figure 9. The blue histogram represents the solutions accounting for constant chord length and the red histogram

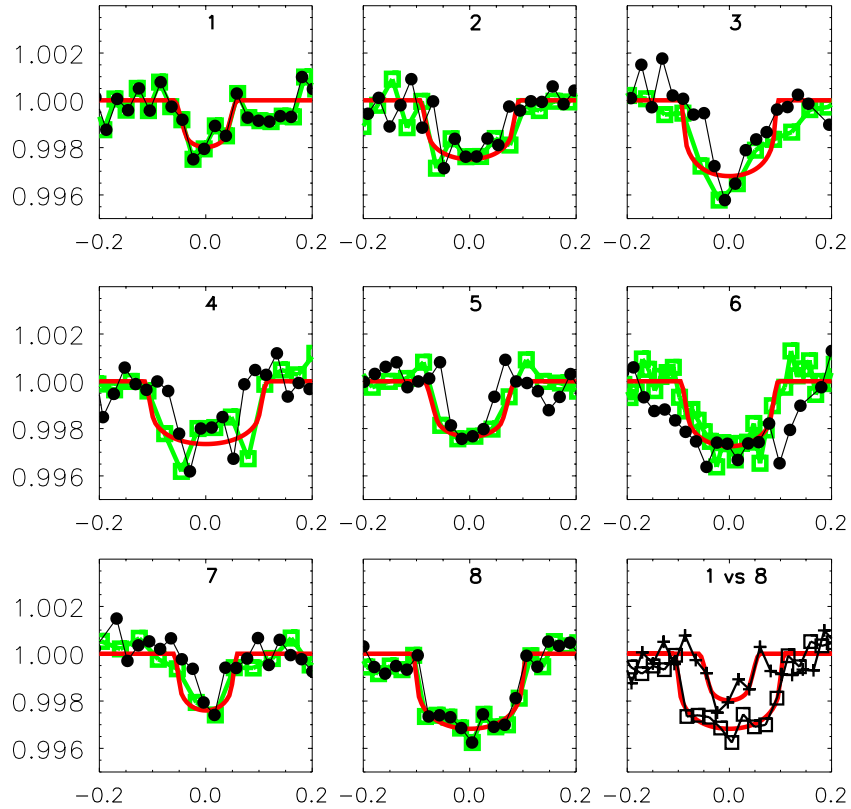


**Figure 7.** Quadratic limb-darkened light curve model fits to the eight scaled transits of Kepler-413b. Black symbols represent observed data, green (or light color) square symbols represent scaled data according to Equation (8), and the red (or gray) curve represents the model fit to the scaled transits. We use the last transit (number 8) as a template for light-curve fitting to estimate  $R_p/R_A$  and  $a_p$ . The binary is near quadrature during transit 8,  $V_{x,A}$  is at its lowest, and the scaling used in Equation (8) is minimal. The result of orbital misalignment is represented in the last panel (“1 vs. 8”), where we compare the two transits (square and cross symbols for transits 8 and 1, respectively) that occur near the same EB phase, but have different impact parameters.

(A color version of this figure is available in the online journal.)

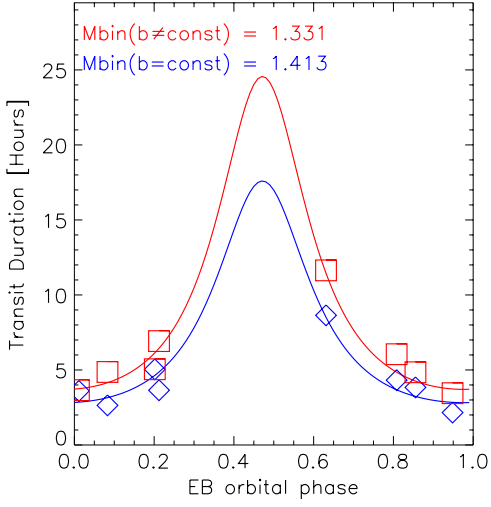


**Figure 8.** CBP transit duration vs. EB phase fits for Kepler-413b using Equation (1). The blue and red curves represent the best fit for constant and for varying impact parameters, respectively. The derived binary mass is 1.41 and 1.33 for the two cases, respectively. The derived primary radius is 0.70 for the blue curve and 0.91 for the red curve. Allowing for a variable impact parameter results in lower and higher estimates of  $M_{\text{bin}}$  and  $R_A$ , respectively, compared with the case of a constant impact parameter.

(A color version of this figure is available in the online journal.)

represents the solutions accounting for variable chord length. The median values for binary mass and their  $1\sigma$  deviations are  $1.41 \pm 0.19$  and  $1.33 \pm 0.17$  for the former and latter case,

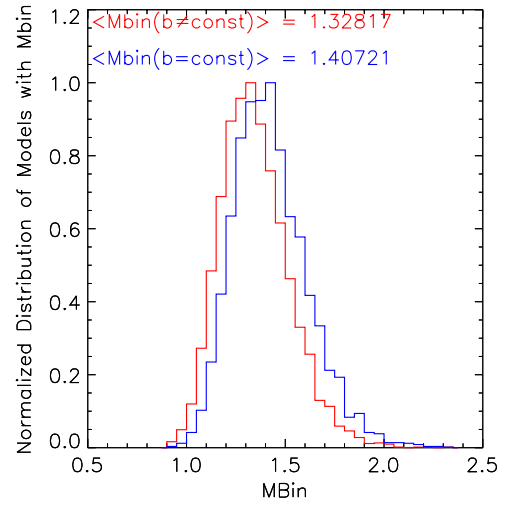


**Figure 9.** Distribution of derived binary masses from Equation (1) for a set of 10,000 scrambled observations. The blue histogram represents the distribution for constant impact parameters for all eight transits and the red histogram represents the distribution for different impact parameters.

(A color version of this figure is available in the online journal.)

respectively. Based on these results, for our preliminary photodynamical search over the parameter space of the Kepler-413 system (described next), we adopt the latter case and allow the binary mass to vary from 1.16 to 1.5.

For our initial photodynamical solutions, we use a numerical  $N$ -body integrator (described in Kostov et al. 2013) to solve the equations of motion. For completeness, we briefly outline it here and discuss the modifications we added for diagnosing Kepler-413. The integrator is an implementation of the SWIFT code<sup>17</sup> adapted for IDL. Due to the particular behavior of the CBP transits of Kepler-413b, we can neither fix the planetary inclination  $i_p$  to  $90^\circ$  nor the ascending node  $\Omega_p$  and the initial phase  $\phi_{0,p}$  to zero. Unlike the case of Kepler-64b described in Kostov et al. (2013), here we solve numerically for these three parameters. Furthermore, it is not optimal to choose the time of the first transit as the starting point of the numerical integration, as Kostov et al. (2013) did. Doing so would introduce an additional parameter—the impact parameter  $b_0$  of the chosen transit. The estimated impact parameters of the individual transits indicated above are too coarse to be used in the photodynamical model. Instead, here we specify initial conditions with respect to the time when the planet is crossing the  $x$ - $y$  plane ( $z_p = 0$ ), approximately three-fourths of a planetary period prior to transit 2, i.e., at  $t_0 = 2,455,014.465430$  (BJD). This allows us to find the true anomaly of the planet ( $\theta_p = 2\pi - \omega_p$ ) and the planet’s eccentric and mean anomalies at the reference time. The number of free parameters we solve for is nine:  $M_A, a_p, e_p, \omega_p, i_p, \Omega_p, \phi_{0,p}, R_A$ , and  $R_p$ .

Restricting the binary mass to the  $1\sigma$  range indicated by the scrambled durations, we fit preliminary photodynamical models to the eight transits of Kepler-413b by performing a grid search over the eight parameters. The quality of the fit is defined as the chi-squared value of the  $O-C$  mid-transit times of all eight events. Starting with an initial coarse timestep of 0.1 days, we select the models that reproduce the mid-transit times of each of the observed eight transits to within 0.05 days and also correctly “miss” all other events by more than  $R_A + R_p$ . Next, we refine the grid search by reducing the timestep to 0.02 days and minimize again. The best-fit model is further promoted for a detailed Markov Chain Monte Carlo (MCMC) exploration, as described in the next section.

#### 4.2. Comprehensive Photometric-dynamical Analysis

The *Kepler* light curve and RV data for Kepler-413 were further modeled using a comprehensive photometric-dynamical model. This model uses a dynamical simulation, assuming only Newton’s equations of motion and the finite speed of light, to predict the positions of the stars and planet at the observed times (e.g., Doyle et al. 2011; Welsh et al. 2012). The parameters of this simulation are functions of the initial conditions and masses of the three bodies and are provided by the preliminary simulations described above. These positions are used as inputs—along with radii, limb darkening parameters, fluxes, and “third-light” contamination—to a code (Carter et al. 2011; Pál 2012) that produces the modeled total flux (appropriately integrated to the *Kepler* “long cadence” exposure). This flux is compared directly with a subset of the full *Kepler* data. The RV data of the larger star are compared with the velocities determined by the dynamical simulation at the observed times.

We isolate only the *Kepler* data within a day of the stellar eclipses or suspected planetary transit crossing events (data involving “missing” events are included as well). Those data, excluding the eclipse features, are divided by a linear function in time in order to detrend the light curve for local astrophysical or systematic features that are unrelated to the eclipses.

The model described in this section has 23 adjustable parameters. Three parameters are associated with the RV data: the RV semi-amplitude of star A,  $K_A$ , the RV offset,  $\gamma_A$ , and a “jitter” term,  $\sigma_{RV}$ , that is added in quadrature to the individual RV errors, correcting for unaccounted systematic error sources. The initial conditions are provided as instantaneous Keplerian elements of the stellar (subscript “bin”) and planetary (subscript “ $p$ ”) orbits, defined in the Jacobian scheme: the periods,  $P_{\text{bin},p}$ , the sky-plane inclinations  $i_{\text{bin},p}$ , vectorial eccentricities  $e_{\text{bin},p} \cos(\omega_{\text{bin},p})$ ,  $e_{\text{bin},p} \sin(\omega_{\text{bin},p})$ , the relative nodal longitude  $\Delta\Omega = \Omega_p - \Omega_{\text{bin}}$ , and the times of barycenter passage  $T_{\text{bin},p}$ . The latter parameters are more precisely constrained by the data than the mean anomalies; however, they may be related to the mean anomalies,  $\eta_{\text{bin},p}$ , via

$$\frac{P_{\text{bin},p}}{2\pi} \eta_{\text{bin},p} = t_0 - T_{\text{bin},p} + \frac{P_{\text{bin},p}}{2\pi} \times [E_{\text{bin},p} - e_{\text{bin},p} \sin(E_{\text{bin},p})], \quad (9)$$

where  $E_{\text{bin},p}$  are the eccentric anomalies at barycenter passage, defined by

$$\tan\left(\frac{E_{\text{bin},p}}{2}\right) = \sqrt{\frac{1 - e_{\text{bin},p}}{1 + e_{\text{bin},p}}} \tan\left(\frac{\pi}{4} - \omega_{\text{bin},p}\right). \quad (10)$$

Two parameters are the mass ratios between stars and planet,  $M_A/M_B$  and  $M_p/M_A$ . The remaining seven parameters are related to the photometric model: the density of star A,  $\rho_A$ , the two radii ratios,  $R_B/R_A$  and  $R_p/R_A$ , the *Kepler*-band flux ratio  $F_B/F_A$ , the linear limb darkening parameter of star A,  $u_1$ , and the additional flux from contaminating sources  $F_X/F_A$ . A final parameter parameterizes the Gaussian distribution of the photometric residuals,  $\sigma_{LC}$ .

We adopted uniform priors in all the parameters excluding the vectorial eccentricities and  $F_X/F_A$ . For those parameters, we enforced uniform priors in  $e_{\text{bin},p}$  and  $\omega_{1,2}$  and a Gaussian prior in  $F_X/F_A$  with mean 0.08 and variance 0.0001. The likelihood of a given set of parameters was defined as

$$L \propto \prod_{i=1}^{N_{LC}} \sigma_{LC}^{-1} \exp\left[-\frac{\Delta L_i^2}{2\sigma_{LC}^2}\right] \times \prod_{i=1}^{N_{RV}} (\sigma_{RV}^2 + \sigma_i^2)^{-1/2} \exp\left[-\frac{\Delta RV_i^2}{2(\sigma_i^2 + \sigma_{RV}^2)}\right], \quad (11)$$

where  $\Delta L_i$  is the residual of the  $i$ th photometric measurement and  $\Delta RV_i$  is the residual of the  $i$ th RV measurement with formal error  $\sigma_i$ .

We explored the parameter space with a Differential Evolution MCMC algorithm (ter Braak & Vrugt 2008). In detail, we generated a population of 60 chains and evolved through approximately 100,000 generations. The initial parameter states of the 60 chains were randomly selected from an over-dispersed region in parameter space bounding the final posterior distribution. The first 10% of the links in each individual Markov chain were clipped and the resulting chains were concatenated to form a single Markov chain, after having confirmed that each chain had converged according to the standard criteria including the Gelman–Rubin convergence statistics and the observation of a long effective chain length in each parameter (as determined from the chain autocorrelation).

The photodynamical fits to the eight observed transits of the CBP are shown in Figure 10. We note that our model predicts

<sup>17</sup> <http://www.boulder.swri.edu/~hal/swift.html>

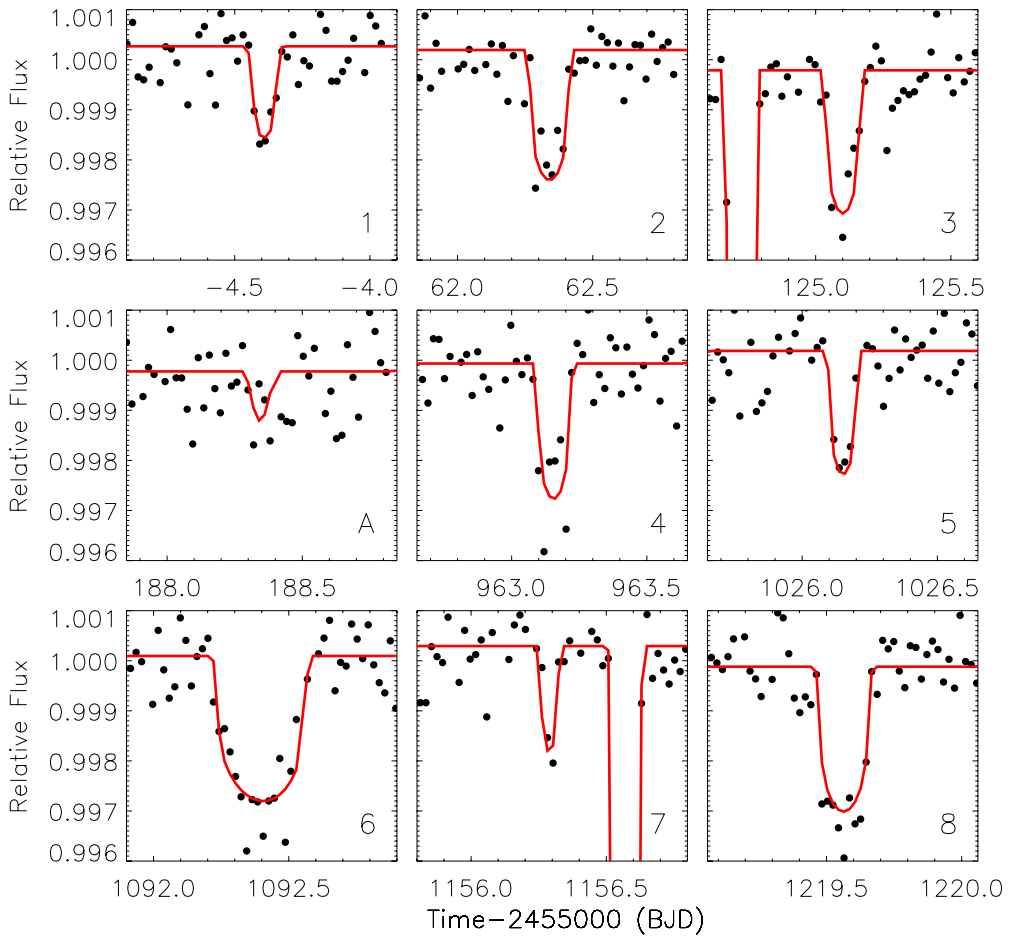


**Figure 10.** Photodynamical fits (red online gray in the printed journal) to the eight observed (and to a predicted ninth transit, labeled “A” near time 188.35 (BJD – 2,455,000), very shallow and buried in the noise) transits (black symbols) for the best-fit model in Tables 3 and 4. Stellar eclipses are also shown at times 124.7 and 1156.5 (BJD – 2,455,000). We note the timescale between transits 3 and 4.

(A color version of this figure is available in the online journal.)

a ninth transit, very shallow and buried in the noise, labeled “A” in Figure 10. For clarity, we label the observed transits with a number and those either missed or not detected with a letter. We tabulate the results of this analysis in Tables 3 and 4, reporting the median and 68% confidence interval for the marginalized distributions in the model parameters and some derived parameters of interest. The parameters we adopt throughout this paper are the “best-fit” values reported in Tables 3 and 4. The observed and predicted mid-transit times, depths, and durations of the planetary transits are shown in Table 5. The orbital configuration of the system is shown in Figure 11. The orbit of the CBP evolves continuously and, due to precession, is not closed. We note that our best-fit mass for the planet is large for its radius. The expected mass is  $M_p \sim 16 M_\oplus$ , using the mass-radius relation of Weiss et al. (2013) for  $1 M_\oplus < M < 150 M_\oplus$ , whereas our model provides  $M_p \sim 67 M_\oplus \pm 21 M_\oplus$ . This suggests that either Kepler-413b is a much denser planet (a mix of rock, metal, gas) or that the mass is even more uncertain than stated and a factor of two to three times likely smaller.

We note that the binary orbit reacts to the gravitational perturbation of the planet. As a result, the EB orbital parameters and eclipse times are not constant. The effect, however, is difficult to measure with the available data. Also, the planetary orbit does not complete one full precession period between transits 1 and 8. The precession period for our best-fit model is

~4000 days, in-line with the analytic estimate of ~4300 days (for equal mass stars) based on Schneider (1994). After transit 8, the transits cease as the planetary orbit precesses away from the favorable transit configuration. The transits will reappear after BJD 2,458,999 (29 May 2020).

#### 4.3. Orbital Stability

The minimum critical semimajor axis (Holman & Wiegert 1999; Equation (3)) for the best-fit parameters of the Kepler-413 system is  $a_{\text{crit}} = 2.55a_{\text{bin}} = 0.26$  AU. With a semimajor axis that is  $\approx 37\%$  larger than the critical limit ( $a_p = 0.3553$  AU), the orbit of the planet Kepler-413b is in a gravitationally stable region. We note that due to the planet’s non-zero eccentricity, its closest approach to the binary is reduced by  $(1 - e)$  and the stability criterion is tighter —  $r_{p,\text{min}} = a_p \times (1.0 - e_p) = 0.3168$  AU, closer compared with a zero-eccentricity orbit, but still beyond  $a_{\text{crit}}$ .

Three-body systems are notorious for exhibiting complex dynamical behavior spurred by mean-motion resonances (MMRs). To explore the long-term stability of the Kepler-413 system, we have studied its dynamical behavior by utilizing the MEGNO<sup>18</sup> factor  $\langle Y \rangle$  (Cincotta & Simó 2000a, 2000b; Cincotta et al. 2003), a widely used method for dynamical analysis of multi-planet systems (Goździewski et al. 2008; Hinse et al. 2010). We note

<sup>18</sup> Mean Exponential Growth of Nearby Orbits.

**Table 3**  
Model Parameters for the Photometric-dynamical Model

Index	Parameter Name	Best-fit	50%	15.8%	84.2%
<i>Mass parameters</i>					
0	RV Semi-amplitude Star A, $K_A$ (km s $^{-1}$ )	43.42	43.49	-0.16	+0.19
1	Mass ratio, Star B, $M_B/M_A$	0.6611	0.6592	-0.0035	+0.0034
2	Planetary mass ratio, $M_p/M_A$ ( $\times 1000$ )	0.245	0.186	-0.078	+0.078
<i>Stellar orbit</i>					
3	Orbital period, $P_{\text{bin}}$ (day)	10.1161114	10.1161185	-0.0000101	+0.0000099
4	Time of barycentric passage, $t_{\text{bin}} - 2,455,000$ (BJD)	8.34898	8.34902	-0.00024	+0.00024
5	Eccentricity parameter, $e_{\text{bin}} \sin(\omega_{\text{bin}})$	-0.0359	-0.0360	-0.0023	+0.0022
6	Eccentricity parameter, $e_{\text{bin}} \cos(\omega_{\text{bin}})$	0.006169	0.006166	-0.000037	+0.000038
7	Orbital inclination, $i_{\text{bin}}$ (deg)	87.332	87.301	-0.060	+0.050
<i>Planetary orbit</i>					
8	Orbital period, $P_p$ (day)	66.262	66.269	-0.021	+0.024
9	Time of barycentric passage, $t_p - 2,455,000$ (BJD)	96.64	96.57	-0.17	+0.16
10	Eccentricity parameter, $\sqrt{e_p} \sin(\omega_p)$	0.3426	0.3435	-0.0033	+0.0031
11	Eccentricity parameter, $\sqrt{e_p} \cos(\omega_p)$	-0.027	-0.022	-0.013	+0.014
12	Orbital inclination, $i_p$ (deg)	89.929	89.942	-0.016	+0.024
13	Relative nodal longitude, $\Delta\Omega_p$ (deg)	3.139	3.169	-0.064	+0.080
<i>Radius/light parameters</i>					
14	Linear limb-darkening parameter, $u_A$	0.599	0.643	-0.036	+0.036
15	Density of Star A, $\rho_A$ (g cm $^{-3}$ )	1.755	1.799	-0.049	+0.066
16	Radius ratio, Star B, $R_B/R_A$	0.624	0.650	-0.032	+0.043
17	Planetary radius ratio, $R_p/R_A$	0.0514	0.0517	-0.0013	+0.0013
18	Stellar flux ratio, $F_B/F_A$ ( $\times 100$ )	5.90	6.40	-0.76	+1.05
<i>Relative contamination</i> , $F_{\text{cont}}/F_A$ ( $\times 100$ )					
19	All seasons	7.6	8.0	-1.0	+1.0
<i>Noise parameter</i>					
20	Long-cadence relative width, $\sigma_{\text{LC}}$ ( $\times 10^5$ )	67.78	67.76	-0.53	+0.54
<i>RV parameters</i>					
21	RV offset, $\gamma$ (km s $^{-1}$ )	-27.784	-27.810	-0.113	+0.098
22	RV jitter, $\sigma_{\text{RV}}$ (km s $^{-1}$ )	0.01	0.17	-0.11	+0.20

**Notes.** We adopt the “best-fit” values as the system’s parameters. The reference epoch is  $t_0 = 2,455,014.46543$  (BJD).

**Table 4**  
Derived Parameters from the Photometric-dynamical Model

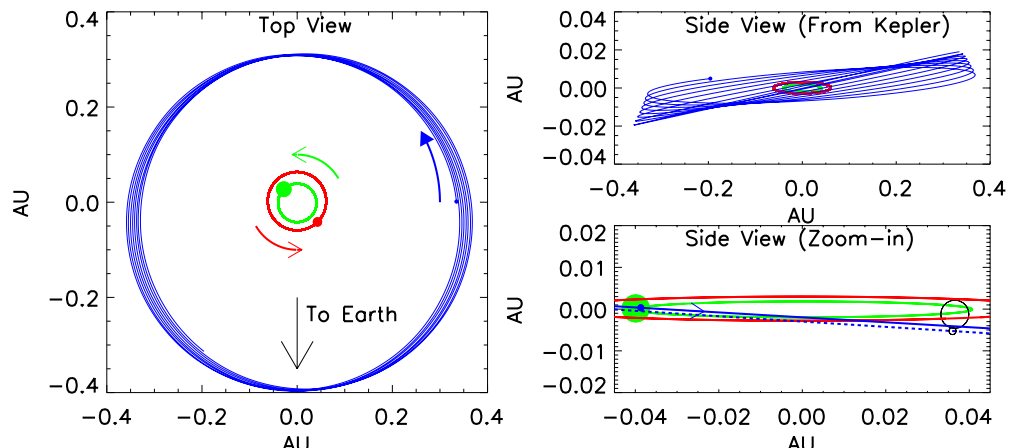
Parameter	Best-fit	50%	15.8%	84.2%
<i>Bulk properties</i>				
Mass of Star A, $M_A$ ( $M_\odot$ )	0.820	0.830	-0.014	+0.015
Mass of Star B, $M_B$ ( $M_\odot$ )	0.5423	0.5472	-0.0073	+0.0081
Mass of Planet b, $M_p$ ( $M_\oplus$ )	67.	51.	-21.	+22.
Radius of Star A, $R_A$ ( $R_\odot$ )	0.7761	0.7725	-0.0096	+0.0088
Radius of Star B, $R_B$ ( $R_\odot$ )	0.484	0.502	-0.021	+0.027
Radius of Planet p, $R_p$ ( $R_\oplus$ )	4.347	4.352	-0.099	+0.099
Density of Star A, $\rho_A$ (g cm $^{-3}$ )	1.755	1.799	-0.049	+0.066
Density of Star B, $\rho_B$ (g cm $^{-3}$ )	4.77	4.32	-0.63	+0.58
Density of Planet, $\rho_p$ (g cm $^{-3}$ )	3.2	2.4	-1.0	+1.0
Gravity of Star A, $\log g_A$ (cgs)	4.5721	4.5811	-0.0086	+0.0108
Gravity of Star B, $\log g_B$ (cgs)	4.802	4.774	-0.046	+0.036
<i>Orbital properties</i>				
Semimajor axis of stellar orbit, $a_{\text{bin}}$ (AU)	0.10148	0.10185	-0.00052	+0.00057
Semimajor axis of planet, $a_p$ (AU)	0.3553	0.3566	-0.0018	+0.0020
Eccentricity of stellar orbit, $e_{\text{bin}}$	0.0365	0.0366	-0.0021	+0.0023
Argument of periape stellar orbit, $\omega_{\text{bin}}$ (deg)	279.74	279.71	-0.58	+0.62
Eccentricity of planetary orbit, $e_p$	0.1181	0.1185	-0.0017	+0.0018
Argument of periape planet orbit, $\omega_p$ (deg)	94.6	93.6	-2.3	+2.2
Mutual orbital inclination, $\Delta i$ (deg) <sup>a</sup>	4.073	4.121	-0.083	+0.113

**Notes.** We adopt the “best-fit” values as the system’s parameters. The reference epoch is  $t_0 = 2,455,014.46543$  (BJD).

<sup>a</sup>  $\cos(\Delta i) = \sin(i_{\text{bin}}) \sin(i_p) \cos(\Delta\Omega) + \cos(i_{\text{bin}}) \cos(i_p)$ .

**Table 5**  
Mid-transit Times, Depths, and Durations of the Planetary Transits

Event #	Center (Time−2,455,000 [BJD])	$\sigma$ (Center)	Depth <sup>a</sup> (ppm)	$\sigma$ (Depth)	Duration (days)	$\sigma$ (Duration)	Center (Time−2,455,000 [BJD])	Duration (days)
<b>Observed</b>							<b>Predicted</b>	
1	−4.3799	0.0019	1557	668	0.1517	0.0113	−4.38	0.14
2	62.3363	0.0018	2134	537	0.18	0.0138	62.34	0.18
3	125.0938	0.0033	2958	678	0.1549	0.0145	125.1	0.16
...	...	...	...	...	...	...	188.34 <sup>b</sup>	0.1
4	963.1529	0.0045	2662	406	0.1551	0.0209	963.16	0.16
5	1026.1544	0.0037	2376	381	0.1083	0.0062	1026.16	0.12
6	1092.3978	0.0075	2759	322	0.3587	0.0199	1092.40	0.36
7	1156.2889	0.0057	1892	394	0.0921	0.0144	1156.29	0.1
8	1219.5674	0.0084	3282	432	0.2149	0.0236	1219.56	0.22
<b>Future</b>								
9	...	...	...	...	...	...	3999.47	0.12

**Notes.**<sup>a</sup> In terms of  $(r_p/r_A)^2$ .<sup>b</sup> Predicted transit; difficult to detect in the data.

**Figure 11.** Orbital configuration of Kepler-413 over the course of one – eight precession period (one-eighth of  $\sim 11$  yr). The orbits of the primary (green or light color) and secondary (red or gray) stars and the CBP (blue or dark color) are to scale in the left and lower-right panels. The EB symbols in the left panel, the CBP symbols, and the vertical axis in the upper-right panel are exaggerated by a factor of 5, 5, and 10, respectively. The EB symbols in the lower-right panel are to scale. The precession of the argument of periastron of the CBP ( $\omega_p$ ) as it increases by  $90^\circ$  is clearly seen in the left panel. Two consecutive passages of the CBP at inferior conjunction are shown in the lower-right panel, demonstrating a missed transit: the solid overlapping symbols (and blue or dark color line for the sky path of the CBP) illustrate the configuration of the system at the last observed transit (transit 8) and, one planetary period later, one missed transit (open symbols for the primary star and the CBP, respectively).

(A color version of this figure is available in the online journal.)

that by a stable orbit here we refer to an orbit that is stable only up to the duration of the numerical integration, i.e., a quasi-periodic orbit. The timescale we use is sufficient to detect the most important MMRs. However, the dynamical behavior of the system past the last integration timestep is unknown.

We utilized the MECHANIC software<sup>19</sup> (Słonina et al. 2012a, 2012b, 2014) to calculate MEGNO maps for Kepler-413, applying the latest MEGNO implementation (Goździewski et al. 2001; Goździewski 2003; Goździewski et al. 2008). The maps have a resolution of  $350 \times 500$  initial conditions in planetary semimajor axis ( $a_p$ ) and eccentricity ( $e_p$ ) space, each integrated for 200,000 days (corresponding to  $\sim 20,000$  binary periods). Quasi-periodic orbits are defined as  $| \langle Y \rangle - 2.0 | \simeq 0.001$ ; for chaotic orbits  $\langle Y \rangle \rightarrow \infty$  as  $t \rightarrow \infty$ . The MEGNO map computed for the best-fit parameters of Table 4 is shown in Figure 12. The cross-hair mark represents the instantaneous

osculating Jacobian coordinates of Kepler-413b. A purple (or dark) color indicates a region of quasi-periodic orbits, whereas a yellow (or light) color denotes chaotic (and possibly unstable) orbits. The CBP sits comfortably in the quasi-periodic (purple) region of  $(a, e)$ -space between the 6:1 and 7:1 MMRs (not unlike Kepler-64b; see Kostov et al. 2013), confirming the plausibility of our solution from a dynamical perspective.

## 5. DISCUSSION

“Why does nature form exoplanets easily?” ponders Heng (2012). Both planetary formation scenarios of core accretion and gravitational collapse require complex processes at work and even more so for the violent environments of CBPs. Yet, the plethora of discovered planets (Burke et al. 2014) indicates that planetary formation is ubiquitous. Martin et al. (2013) argue that it may be in fact easier to form planetary systems around close binary stars than around single stars, if there is a quiescent, low-turbulence layer present in the mid-plane of the CB disks.

<sup>19</sup> <https://github.com/mslonina/Mechanic>

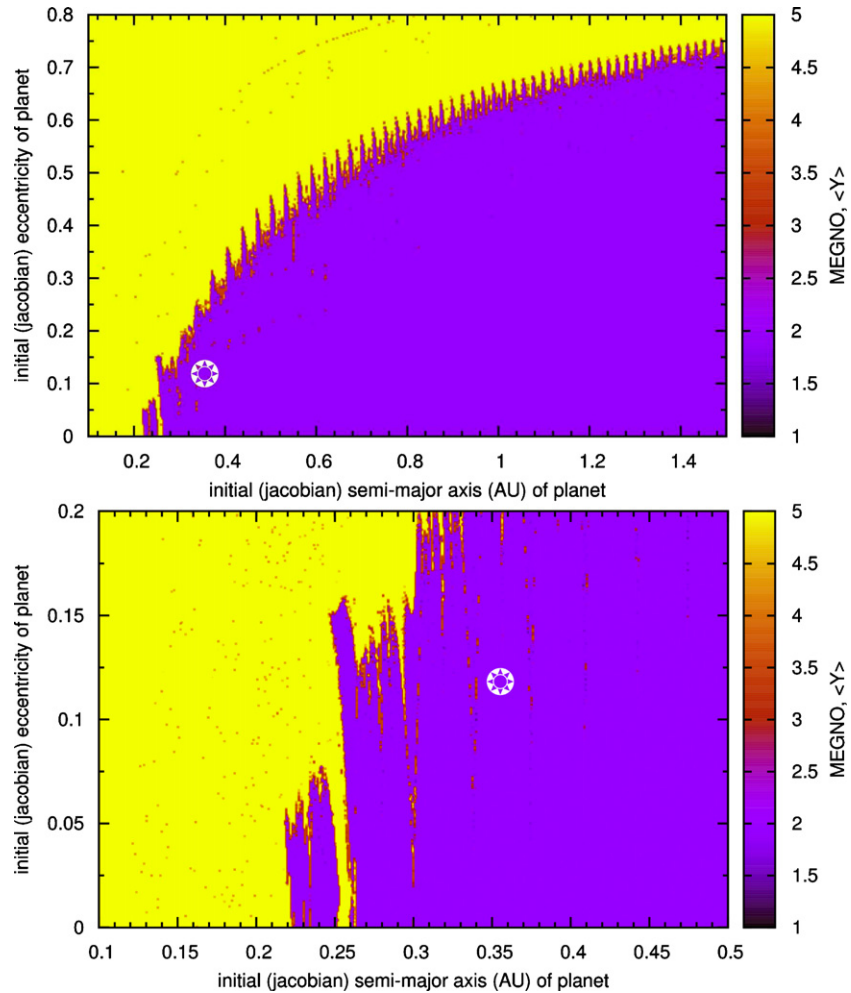


**Figure 12.** Upper panel: MEGNO map of Kepler-413b, using the best-fit parameters from Table 4. A purple (or dark) color outlines quasi-periodic regions in  $(a, e)$ -space and a yellow (or light) color outlines chaotic (and possibly unstable) regions (see the text for details). The cross-hair mark denotes the instantaneous Jacobian coordinates of the planet, placing it firmly in a quasi-periodic orbit and confirming our solution from a dynamical perspective. Lower panel: same as the upper panel, but zoomed-in on a smaller region around the  $(a, e)$  of the planet, confirming its location in the quasi-stable region.

(A color version of this figure is available in the online journal.)

Unlike disks around single stars, the surface density in a CB disk peaks in such a “dead zone” and, being close to the snow line, provides an ideal site for planetary formation. In addition, Alexander (2012) has shown that CB disks around binary stars with  $a_{\text{bin}} < 1$  AU persist longer than disks around single stars, suggesting that formation of CBPs should be commonplace.

The  $\Delta i \sim 2.5^\circ$  misalignment of Kepler-413b is notably larger than that of the other *Kepler*-discovered CBPs (with an average of  $\sim 0.3^\circ$ ). It is, however, comparable to the mutual inclination between Kepler-64b and its host EB, the only known quadruple stellar system with a CBP. It is comparable to the mutual orbital inclinations of  $1^\circ$ – $2.3^\circ$  reported for the *Kepler* and HARPS multi-planet systems orbiting single stars and the solar system value of  $2.1^\circ$ – $3.1^\circ$ , including Mercury (Fabrycky et al. 2012; Fang & Margot, 2012; Figueira et al. 2012; Lissauer et al. 2011).

Quillen et al. (2013) argue that one plausible scenario responsible for the excitation of planetary inclinations is collisions with embryos. The authors note that measured correlations between planetary mass and inclination can provide strong clues for this scenario. While planetary masses are difficult to measure, photodynamical models of slightly misaligned CBPs like Kepler-413b can provide an important venue to test this hypothesis by providing constraints on masses and inclinations. Additionally,

according to Rappaport et al. (2013), up to 20% of close binaries have a tertiary stellar companion, based on extrapolation from ETVs measured for the entire *Kepler* EB catalog. Eggleton & Tokovinin (2008) find that  $\sim 25\%$  of all multiple systems with a solar-type star are triples and higher order. A tertiary companion on a wide orbit can be responsible for complex dynamical history of the binary system involving Kozai cycles with tidal friction (Kozai 1962; Fabrycky & Tremaine 2007; Kiseleva et al. 1998; Eggleton & Kiseleva-Eggleton 2001; Pejcha et al. 2013).

A robust correlation between occurrence rate of planets and (single) host star metallicities has been established over the past 10 yr (Mayor et al. 2011; Howard 2013). While it is equally likely to detect small planets around stars with a wide metallicity range, giant planets ( $R > 4 R_{\text{Earth}}$ ; Howard 2013) are preferentially found in orbits around metal-rich stars. Such dichotomy naturally originates from the core-accretion scenario for planet formation, with the caveat that *in situ* formation may be more appropriate to describe the presence of low-mass planets close to their star (Howard 2013). It is interesting to note that seven of the *Kepler* CB planets are gas giants, with  $R \geq 4.3 R_{\text{Earth}}$ , (the only exception being Kepler 47b), but all seven host stellar systems that are deficient in metals compared with the Sun.

EB systems have long been proposed to be well-suited candidates for the discovery of transiting planets due to the favorable orbital orientation of the stellar system. However, EBs may not be as favorable as generally thought. Given the correct orientation, planets orbiting single stars will transit at every inferior conjunction. As we have shown here, and also discussed by Schneider (1994), misaligned CBPs, however, may either transit or miss depending on their instantaneous orbital configuration. If the configuration is favorable, one can observe several consecutive transits. Otherwise, there may be a few, widely separated transits or even only a single transit. A trivial case is no transits at all during the course of the observations, where the planetary orbit has not yet precessed into the favorable transit geometry and the first “good hit” may be approaching; even a very misaligned system will occasionally transit. Thus, a non-detection of tertiary transits in the light curve of an EB does not rule out the possibility of observing a transiting CBP in the future. This statement is trivially obvious for planets with periods much longer than the duration of observations. However, as this work has illustrated, the statement also applies to short-period planetary orbits with non-zero mutual inclinations.

Such photodynamical effects may further affect the deduced occurrence rate of CBPs, even after accounting for detection efficiency, systematic effects, etc. Aligned systems have a strong selection effect, but many systems (potentially a “silent majority” of CBPs) could be misaligned and precessing and Kepler-413b will be the prototype of that class of objects.

“...The existence of planets in these systems [CBP]...,” Paardekooper et al. (2012, p.1) note, “...baffles planet formation theory....” The fact that the confirmed CBPs are so close to the theoretical limit for dynamical stability and that shorter-period EBs have typically longer-period CBPs (further away from the critical limit) hint at an interesting dynamical history and can be directly addressed by finding more CB systems. Future additions to the still-small family of CBPs will add important new insights to our understanding of these remarkable objects. Or, perhaps more interestingly, the new discoveries will baffle the theoretical framework even further.

### 5.1. Stellar Insolation

Our best-fit photodynamical model places Kepler-413b on a 0.355 AU orbit around two stars with effective temperatures of  $T_A = 4700$  K, estimated from SOPHIE, and  $T_B = 3460$  K, derived from the temperature ratio  $T_B/T_A$  from ELC (see Table 1). The combined incident flux  $S_{\text{tot}} = S_A + S_B$  due to the two stars A and B at the orbital location of Kepler-413b is shown in Figure 13. It varies from a minimum of  $\sim 1.64 S_\star$  to a maximum of  $\sim 3.86 S_\star$  (where  $S_\star$  is the mean solar constant of  $1368 \text{ W m}^{-2}$ ) on two different timescales (stellar and planetary periods), with an average of  $\sim 2.42 S_\star$ . Following Kane & Hinkel (2013), we calculate the effective temperature of the EB,  $T_{\text{eff,AB}}$ , as that of a source with an energy flux similar to that of the two stars combined. From Wien’s displacement law and using the combined blackbody radiation of the two stars, we estimate  $T_{\text{eff,AB}} \sim 4500$  K. Following the cloud-free models of Kopparapu et al. (2013), the inner edge of the habitable zone (“runaway greenhouse”) for the Kepler-413 system is at an incident stellar flux  $S_{\text{inner}} = 0.91 S_\star$  (red or gray line in Figure 13); the outer edge (“maximum greenhouse”) is at  $S_{\text{outer}} = 0.28 S_\star$  (blue or dark line in Figure 13). Kepler-413b is slightly closer to its host star than the inner edge of the habitable zone. We note that the inner edge distance for the habitable zone of the Kepler-413 system for dry, desert planets

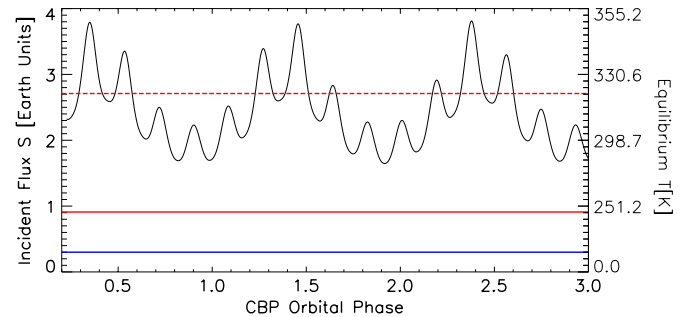


**Figure 13.** Bolometric luminosity in units of  $S_\star = 1368 \text{ W m}^{-2}$  (the mean solar constant), incident at the orbital location of Kepler-413b (black line), as a function of the orbital phase of the planet and equilibrium temperature for a Bond albedo of 0.34. The CBP orbital phase is defined as  $\phi_p = t / P_p$ , with  $\phi_p = 0$  at  $t_0 = 2,455,014.46543$  (BJD). The planet is slightly closer to its host stars than the inner edge of the habitable zone, which is at  $S_{\text{inner}} = 0.91 S_\star$ . For comparison, we show the inner (red line) and outer (blue line) edges of the habitable zone of Kepler-413. The dashed line indicates the inner edge of the dry-desert habitable zone,  $S_{\text{inner,desert}} = 2.71 S_\star$ ; the planet is in the dry-desert habitable zone for most of its orbit.

(A color version of this figure is available in the online journal.)

is at  $\sim 0.32$  AU (Equation (12); Zsom et al. 2013),  $\sim 2.71 S_\star$ , for a surface albedo of 0.2 and 1% relative humidity. This limiting case places Kepler-413b ( $a_p = 0.3553$  AU) in the dry-desert habitable zone for most of its orbit.

The flux variations experienced by the CBP, coupled with the peculiar behavior of the planetary obliquity described next, may result in very interesting and complex weather and climate patterns on Kepler-413b and similar CBPs.

### 5.2. Cassini States

Next, we discuss how the quick orbital precession, which is highly constrained by the transit fits, should affect the spin orientation of Kepler-413b. Instantaneously, each of the stars causes a torque on the rotational bulge of the planet, but over one EB orbit, and even over one orbit of the CBP, this torque causes little reorientation of the planet. Over many orbits, however, the effect of this torque adds coherently. If we replace the stars with a point mass at their barycenter, the small-obliquity precession angular frequency of the planetary spin would be (e.g., Fabrycky et al. 2007)

$$\alpha = \frac{k_{2,p}}{c_p} \frac{M_A + M_B}{M_p} (1 - e_p^2)^{-3/2} (R_p/a_p)^3 S_p, \quad (12)$$

where  $k_{2,p}$  is the apsidal motion constant (half the Love number) of the CBP,  $c_p$  is the normalized moment of inertia, and  $S_p$  is the spin angular frequency of the planet.

In the presence of quick orbital precession, the dynamics become much richer, as Cassini States appear (Ward & Hamilton 2004; Hamilton & Ward 2004; Fabrycky et al. 2007; Levrard et al. 2007). These states are fixed points of the spin dynamics in which the spin and orbit precess at the same rate around the total angular momentum. Thus, the effect is a 1:1 secular resonance between the orbital precession and the spin precession. The orbital precession rate,  $g$ , is known from the best-fitting model:  $g = 0.57 \text{ radians yr}^{-1}$ . Taking a one-day rotation period (i.e.,  $S_p = 2\pi \text{ radians/day}$ ) for Kepler-413b,  $k_{2,p} = 0.1$ ,  $c_p = 0.08$ , and assuming  $M_p = 15 M_\oplus$ , with the above values of the constants, we have  $\alpha = 1.0 \text{ radians yr}^{-1}$ , very close to resonant with  $g$ . Even precession trajectories that are not in these states are affected by them, as they must navigate the resonant island.

Thus, when  $\alpha \approx g$ , the obliquity can vary by many degrees on a timescale somewhat longer than the precession timescale.

However, the value of  $\alpha$  for the case of Kepler-413b is very uncertain due to the poorly constrained parameters, particularly  $M_p$  and  $S_p$ . For the best-fitting  $M_p$  of  $\sim 60 M_\oplus$  (and other parameters as assumed above), the spin would travel around Cassini State 2 (see Peale 1969 for the numbering), the state in which the spin responds to torques more slowly than the orbit precesses. In that case, the spin feels the precession-averaged effect of the EB orbit and so its spin-precession pole is close to the orbit normal of the binary (the dominant angular momentum). This is the case for the Earth’s moon, which has faster orbital precession than spin precession and it is tidally damped to Cassini State 2. If Kepler-413b has instead low mass,  $M_p < 10 M_\oplus$  (i.e., quite puffy), it could have a higher natural spin frequency  $\alpha$ . In that case, it is possible for the planet to be in a tipped-over Cassini State 2, in which a high obliquity (near  $90^\circ$ ) lessens the torque from the binary star, allowing the planet precession to continue resonating with the orbital precession. However, it is more likely that it would travel around Cassini State 1, which is the normal precession around an orbit, but slightly modified due to the (relatively slow) precession of that orbit. Finally, for the Neptune-like mass of  $15 M_\oplus$  assumed above, both Cassini State 1 and Cassini State 2 would be considerably displaced from the orbit normal and either large obliquity or large obliquity fluctuations ( $\sim 30^\circ$ ) would result.

It is beyond the scope of this work to calculate the obliquity evolution of Kepler-413b in detail. We expect, however, that it would give interesting boundary conditions for climate models (Langton & Laughlin 2007). Another consideration is that the  $\alpha$  value would have changed as the planet cooled, as that contraction would result in changes in  $R_p$ ,  $k_{2,p}$ ,  $c_p$ , and  $S_p$ ; the scanning of  $\alpha$  could cause trapping into a Cassini resonance (Winn & Holman 2005). We expect that at the orbital distance of Kepler-413b, tides would be too weak to cause spin alignment, but we note that in other systems such alignment would bring the planetary spin to a Cassini State rather than standard spin-orbit locking (Fabrycky et al. 2007).

Finally, we suggest that spin precession of a planet may actually be observable for CBP systems. Carter & Winn (2010) pointed out that a precessing planet will display a time-varying surface area to a transit observer, due to the oblateness of the planet changing orientations. A Saturn-like oblateness with a  $30^\circ$  obliquity results in a few-percent change in depth over the precession cycle. The radii ratios in some CBP systems are constrained by *Kepler* photometry at the  $\sim 1\%$  level, thus variations at this level might be detectable. This is considerably more observable than the transit shape signature of oblique planets (Seager & Hui 2002; Barnes & Fortney 2003).

## 6. CONCLUSIONS

We report the discovery of a  $R_p = 4.347 \pm 0.099 R_\oplus$  planet transiting the primary star of Kepler-413. The system consists of two K+M stars that eclipse each other every 10.116148 days. Due to the small misalignment ( $\Delta i \sim 2.5^\circ$ ) between the binary and CBP orbital planes, the latter precesses and the planet often fails to transit the primary star. The CBP revolves around the EB every  $\sim 66$  days on an orbit with  $a_p = 0.355$  AU and  $e = 0.118 \pm 0.002$ . The orbital configuration of the system is such that we observe a set of three transits occurring  $\sim 66$  days apart, followed  $\sim 800$  days later by five more transits also separated by  $\sim 66$  days from each other. We note that, among

the known transiting CBPs, Kepler-413b is the only CBP with a higher eccentricity compared with its host binary star.

Spectroscopic measurements determined the target as a single-lined EB and provided its mass function, eccentricity, and argument of periastron. Photometric observations identified a nearby companion (“third light”) to Kepler-413 inside the central *Kepler* pixel and addressed its flux contamination to the target’s light curve (V. B. Kostov et al. 2014, in preparation). Based on statistical estimates, we propose that the companion star is gravitationally bound to the EB, making Kepler-413b a CBP in a triple stellar system.

Our best-fit model places Kepler-413b slightly closer to its host stars than the inner edge of the extended habitable zone, with the bolometric insolation at the location of the planet’s orbit varying between  $\sim 1.75 S_\star$  and  $\sim 3.9 S_\star$  on multiple timescales (where  $S_\star = 1368 \text{ W m}^{-2}$ , the mean solar constant). The planet is, however, in the dry-desert habitable zone for most of its orbit. Also, the peculiar orbital configuration of the system indicates that KIC123b may be subject to Cassini State dynamics. Depending on the angular precession frequency of the planet, its spin and orbital precession rates could be commensurate. This suggests that Kepler-413b may experience obliquity fluctuations of dozens of degrees on precession timescales ( $\sim 11$  yr) and complex seasonal cycles with interesting climate patterns.

The transits of a CBP provide precise measurements of the stellar and planetary sizes and of the masses of the host binary star. Our discovery adds to the growing knowledge about CBPs: their radii, masses, occurrence frequency about different types of stars, when they formed (first versus second generation), and even whether the concept of habitability can be extended beyond single-star planetary systems. The results reported here can be applied to studies of the formation and evolution of protoplanetary disks and planetary systems in multiple-stellar systems.

This research was performed in partial fulfillment of the requirements of the Ph.D. of V.B.K. at Johns Hopkins University. The authors gratefully acknowledge everyone who has contributed to the *Kepler* Mission, which is funded by NASA’s Science Mission Directorate. We acknowledge conversations with Nicolas Crouzet, Holland Ford, K. Goździewski, Nader Haghighipour, Amy McQuillan, Colin Norman, Rachel Osten, Neill Reid, Jean Schneider, M. Słonina, and Martin Still. The authors thank the referee for the helpful comments and suggestions.

This research used observations made with the SOPHIE instrument on the 1.93 m telescope at Observatoire de Haute-Provence (CNRS), France, as part of programs 12B.PNP.MOUT and 13A.PNP.MOUT. This research made use of the SIMBAD database, operated at CDS, Strasbourg, France; data products from the Two Micron All Sky Survey (2MASS), the Digitized Sky Survey (DSS), the NASA exoplanet archive NexSci<sup>20</sup>, source code for transit light curves (Mandel & Agol 2002), and the SFI/HEA Irish Centre for High-End Computing (ICHEC). Numerical computations presented in this work were partly carried out using the SFI/HEA Irish Centre for High-End Computing (ICHEC, STOKES) and the PLUTO computing cluster at KASI; astronomical research at Armagh Observatory is funded by the Department of Culture, Arts and Leisure (DCAL). V.B.K. and P.R.M. received funding from a NASA Origins of Solar Systems grant NNX10AG30G and NESSF

<sup>20</sup> <http://exoplanetarchive.ipac.caltech.edu>

grant NNX13AM33H. W.F.W. and J.A.O. gratefully acknowledge support from the National Science Foundation via grant AST-1109928 and from NASA's *Kepler* Participating Scientist Program (NNX12AD23G) and Origins of Solar Systems Program (NNX13AI76G). T.C.H acknowledges support by the Korea Research Council for Science and Technology (KRCF) through the Young Scientist Research Fellowship Program grant number 2013-9-400-00. T.M. acknowledges support from the European Research Council under the EU's Seventh Framework Programme (FP7/(2007-2013)/ERC Grant Agreement No. 291352) and from the Israel Science Foundation (grant No. 1423/11).

## REFERENCES

- Adams, E. R., Ciardi, D. R., Dupree, A. K., et al. 2012, *AJ*, **144**, 42  
 Alexander, R. 2012, *ApJ*, **757**, 29  
 Baranec, C., Riddle, R., Law, N. M., et al. 2013, *J. Vis. Exp.*, **72**, e50021  
 Baranne, A., Queloz, D., Mayor, M., et al. 1996, *A&AS*, **119**, 373  
 Barnes, J. W., & Fortney, J. J. 2003, *ApJ*, **588**, 545  
 Borkovits, T., Derekas, A., Kiss, L. L., et al. 2012, *MNRAS*, **428**, 1656  
 Bouchy, F., Hébrard, G., Udry, S., et al. 2009, *A&A*, **505**, 853  
 Burke, C. J., Bryson, S. T., Mullaly, F., et al. 2014, *ApJS*, **210**, 2  
 Burke, C. J., Gaudi, B. S., DePoy, D. L., & Pogge, R. W. 2006, *AJ*, **132**, 210  
 Carter, J. A., Fabrycky, D. C., Ragozzine, D., et al. 2011, *Sci*, **331**, 562  
 Carter, J. A., & Winn, J. N. 2010, *ApJ*, **716**, 850  
 Cincotta, P. M., Giordano, C. M., & Simó, C. 2003, *PhyD*, **182**, 151  
 Cincotta, P. M., & Simó, C. 2000a, *CeMDA*, **73**, 195  
 Cincotta, P. M., & Simó, C. 2000b, *A&AS*, **147**, 205  
 Clanton, C. 2013, *ApJ*, **768**, 15  
 Díaz, R. F., Damiani, D., Deleuil, M., et al. 2013, *A&A*, **551**, L9  
 Doyle, L. R., Carter, J. A., Fabrycky, D. C., et al. 2011, *Sci*, **333**, 6049  
 Eggleton, P. P., & Kiseleva-Eggleton, L. 2001, *ApJ*, **562**, 1012  
 Eggleton, P. P., & Tokovinin, A. A. 2008, *MNRAS*, **389**, 869  
 Fabrycky, D. C., Johnson, E. T., & Goodman, J. 2007, *ApJ*, **665**, 754  
 Fabrycky, D. C., Lissauer, J. J., Ragozzine, D., et al. 2012, arXiv:1202.6328  
 Fabrycky, D. C., & Tremaine, S. 2007, *ApJ*, **669**, 1289  
 Fang, J., & Margot, J.-L. 2012, *ApJ*, **761**, 2  
 Figueira, P., Marmier, M., Boue, G., et al. 2012, *A&A*, **541**, 10  
 Foucart, F., & Lai, D. 2013, *ApJ*, **764**, 106  
 Gilliland, R. L., Chaplin, W. J., Dunham, E. W., et al. 2011, *ApJS*, **197**, 6  
 Goździewski, K. 2003, *A&A*, **398**, 315  
 Goździewski, K., Bois, E., Maciejewski, A. J., & Kiseleva-Eggleton, L. 2001, *A&A*, **378**, 569  
 Goździewski, K., Breiter, S., & Borczyk, W. 2008, *MNRAS*, **383**, 989  
 Hamilton, D. P., & Ward, W. R. 2004, *ApJ*, **128**, 2510  
 Hébrard, G., Amenara, J.-M., Santerne, A., et al. 2013, *A&A*, **554**, A114  
 Hébrard, G., Bouchy, F., Pont, F., et al. 2008, *A&A*, **488**, 763  
 Heng, K. 2012, arXiv:1304.6104  
 Hilditch, R. W. 2001, An Introduction to Close Binary Stars (Cambridge: Cambridge Univ. Press), **392**  
 Hinse, T. C., Christou, A. A., Alvarellos, J. L. A., & Goździewski, K. 2010, *MNRAS*, **404**, 837  
 Holman, M. J., & Wiegert, P. A. 1999, *AJ*, **117**, 621  
 Howard, A. W. 2013, *Sci*, **340**, 572  
 Jenkins, J. M., Caldwell, D. A., Chandrasekaran, H., et al. 2010a, *ApJ*, **713**, 87  
 Jenkins, J. M., Caldwell, D. A., Chandrasekaran, H., et al. 2010b, *ApJL*, **713**, L120  
 Kane, S. R., & Hinkel, N. R. 2013, *ApJ*, **762**, 7  
 Kinemuchi, K., Barclay, T., Fanelli, M., et al. 2012, *PASP*, **124**, 963  
 Kiseleva, L. G., Eggleton, P. P., & Mikkola, S. 1998, *MNRAS*, **300**, 292  
 Kopparapu, R. K., Ramirez, R., Kasting, J. F., et al. 2013, *ApJ*, **765**, 131  
 Kostov, V. B., McCullough, P. R., Hinse, T. C., et al. 2013, *ApJ*, **770**, 52  
 Kovács, G., Zucker, S., & Mazeh, T. 2002, *A&A*, **391**, 369  
 Kozai, Y. 1962, *AJ*, **67**, 591  
 Langton, J., & Laughlin, G. 2007, *ApJ*, **657**, 113  
 Lawrence, A., Warren, S. J., Almaini, O., et al. 2007, *MNRAS*, **379**, 1599  
 Levrad, B., Correia, A. C. M., Chabrier, G., et al. 2007, *A&A*, **462**, 5  
 Lillo-Box, J., Barrado, D., & Bouy, H. 2012, *A&A*, **546**, 10  
 Lissauer, J. J., Ragozzine, D., Fabrycky, D. C., et al. 2011, *ApJS*, **197**, 8  
 Loeb, A., & Gaudi, B. S. 2003, *ApJL*, **588**, L117  
 Mandel, K., & Agol, E. 2002, *ApJL*, **580**, L171  
 Martin, R. G., Armitage, P. J., & Alexander, R. D. 2013, *ApJ*, **773**, 74  
 Marzari, F., Thebault, P., Scholl, H., et al. 2013, *A&A*, **553**, 71  
 Mayor, M., Marmier, M., Lovis, C., et al. 2011, arXiv:1109.2497  
 McQuillan, A., Aigrain, S., & Mazeh, T. 2013a, *MNRAS*, **432**, 1203  
 McQuillan, A., Mazeh, T., & Aigrain, S. 2013b, *ApJL*, **775**, 11  
 Meixner, M., Smee, S., Doering, R. L., et al. 2010, *PASP*, **122**, 451  
 Meschiari, S. 2012a, *ApJ*, **752**, 71  
 Meschiari, S. 2012b, *ApJ*, **761**, 7  
 Meschiari, S. 2013, arXiv:1309.4679  
 Orosz, J. A., Welsh, W. F., Carter, J. A., et al. 2012a, *Sci*, **337**, 1511  
 Orosz, J. A., Welsh, W. F., Carter, J. A., et al. 2012b, *ApJ*, **758**, 87  
 Paardekooper, S.-J., Leinhardt, Z. M., Thibault, P., & Baruteau, C. 2012, *ApJ*, **754**, 16  
 Pál, A. 2012, *MNRAS*, **420**, 1630  
 Peale, S. J. 1969, *AJ*, **74**, 483  
 Pejcha, O., Antognini, J. M., Shappee, B. J., & Thompson, T. A. 2013, *MNRAS*, **435**, 943  
 Pepe, F., Mayor, M., Galland, F., et al. 2002, *A&A*, **388**, 632  
 Pierens, A., & Nelson, R. P. 2007, *A&A*, **472**, 993  
 Pierens, A., & Nelson, R. P. 2008a, *A&A*, **478**, 939  
 Pierens, A., & Nelson, R. P. 2008b, *A&A*, **482**, 333  
 Pierens, A., & Nelson, R. P. 2008c, *A&A*, **483**, 633  
 Pierens, A., & Nelson, R. P. 2013, *A&A*, **556**, 134  
 Prša, A., Batalha, N., Slawson, R. W., et al. 2011, *AJ*, **141**, 83  
 Quillen, A. C., Bodman, E., & Moore, A. 2013, *MNRAS*, **435**, 2256  
 Quintana, E. V., & Lissauer, J. J. 2006, *Icar*, **185**, 1  
 Rafikov, R. 2013, *ApJ*, **764**, 16  
 Rappaport, S., Deck, K., Levine, A., et al. 2013, *ApJ*, **768**, 33  
 Rybicki, G. B., & Lightman, A. P. 1985, Radiative Processes in Astrophysics (New York: Wiley)  
 Santerne, A., Bonomo, A. S., Hébrard, G., et al. 2011, *A&A*, **536**, A70  
 Schneider, J. 1994, *P&SS*, **42**, 539  
 Schwamb, M. E., Orosz, J. A., Carter, J. A., et al. 2013, *ApJ*, **768**, 127  
 Seager, S., & Hui, L. 2002, *ApJ*, **574**, 1004  
 Seager, S., & Mallén-Ornelas, G. 2003, *ApJ*, **585**, 1038  
 Skrutskie, M. F., Cutri, R. M., Stiening, R., et al. 2006, *AJ*, **131**, 2  
 Slawson, R. W., Prša, A., Welsh, W. F., et al. 2011, *AJ*, **142**, 160  
 Ślōnina, M., Goździewski, K., & Migaszewski, C. 2012a, in Proc. Workshop Orbital Couples: Pas de Deux in the Solar System and Milky Way, ed. F. Arenou & D. Hestroffer, 125  
 Ślōnina, M., Goździewski, K., Migaszewski, C., & Rozenkiewicz, A. 2012b, *MNRAS*, submitted, arXiv:1205.1341S  
 Ślōnina, M., Goździewski, K., Migaszewski, C., & Rozenkiewicz, A. 2014, NewA, submitted  
 Still, M., & Barclay, T. 2012, Astrophysics Source Code Library, record ascl:1208.004  
 ter Braak, C. J. F., & Vrugt, J. A. 2008, *Stat. Comput.*, **16**, 239  
 Tokovinin, A., Thomas, S., Sterzik, M., & Udry, S. 2006, *A&AS*, **450**, 681  
 Torrence, C., & Compo, G. P. 1998, *BAMS*, **79**, 61  
 Ward, W. R., & Hamilton, D. P. 2004, *ApJ*, **128**, 2501  
 Weiss, L. M., Marcy, G. W., Rowe, J. F., et al. 2013, *ApJ*, **768**, 14  
 Welsh, W. F., Orosz, J. A., Carter, J. A., et al. 2012, *Natur*, **481**, 475  
 Winn, J. N., & Holman, M. 2005, *ApJ*, **628**, 159  
 Zsom, A., Seager, S., de Wit, J., & Stamenkovic, V. 2013, *ApJ*, **778**, 109

ERRATUM: “KEPLER-413B: A SLIGHTLY MISALIGNED, NEPTUNE-SIZE TRANSITING CIRCUMBINARY PLANET” (2014, ApJ, 784, 14)

V. B. KOSTOV<sup>1,2,12</sup>, P. R. McCULLOUGH<sup>1,2</sup>, J. A. CARTER<sup>3,13</sup>, M. DELEUIL<sup>4</sup>, R. F. DÍAZ<sup>4</sup>, D. C. FABRYCKY<sup>5</sup>, G. HÉBRARD<sup>6,7</sup>, T. C. HINSE<sup>8,9</sup>, T. MAZEH<sup>10</sup>, J. A. OROSZ<sup>11</sup>, Z. I. TSVETANOV<sup>1</sup>, AND W. F. WELSH<sup>11</sup>

<sup>1</sup> Department of Physics and Astronomy, Johns Hopkins University, 3400 North Charles Street, Baltimore, MD 21218, USA; [vkostov@pha.jhu.edu](mailto:vkostov@pha.jhu.edu)

<sup>2</sup> Space Telescope Science Institute, 3700 San Martin Drive, Baltimore, MD 21218, USA

<sup>3</sup> Harvard-Smithsonian Center for Astrophysics, 60 Garden Street, Cambridge, MA 02138, USA

<sup>4</sup> Laboratoire d’Astrophysique de Marseille, 38 rue Frédéric Joliot-Curie, F-13388 Marseille Cedex 13, France

<sup>5</sup> Department of Astronomy and Astrophysics, University of Chicago, 5640 South Ellis Avenue, Chicago, IL 60637, USA

<sup>6</sup> Institut d’Astrophysique de Paris, UMR 7095 CNRS, Université Pierre et Marie Curie, 98bis Boulevard Arago, F-75014 Paris, France

<sup>7</sup> Observatoire de Haute-Provence, Université d’Aix-Marseille et CNRS, F-04870 Saint Michel l’Observatoire, France

<sup>8</sup> Korea Astronomy and Space Science Institute (KASI), Advanced Astronomy and Space Science Division, Daejeon 305-348, Korea

<sup>9</sup> Armagh Observatory, College Hill, Armagh BT61 9DG, NI, UK

<sup>10</sup> Department of Astronomy and Astrophysics, Tel Aviv University, 69978 Tel Aviv, Israel

<sup>11</sup> Department of Astronomy, San Diego State University, 5500 Campanile Drive, San Diego, CA 92182, USA

Received 2014 March 23; published 2014 May 6

Due to an error at the publisher, the published article contains a numerical error in the calculation of the spin precession rate of the planet (Section 5.2). The error overestimates the fixed-point obliquity of the planet, with the implication that only Cassini State 2 is relevant for the spin dynamics of the system. In this state, the spin responds to torques more slowly than the orbit precesses.

The correct natural spin precession rate of the planet is  $\alpha = 0.02 \text{ rad yr}^{-1}$  (Equation (12), using a 16 hr Neptune-like rotation period), considerably less than the orbital precession rate  $g$ . The spin feels the precession-averaged effect of the eclipsing binary orbit, and so the spin-precession pole of the planet is close to the orbit normal of the binary (the dominant angular momentum) and oscillates at the orbital precession frequency of 11 yr. This is the case of the Earth’s moon, whose orbit around the Earth precesses quickly due to solar perturbations, much faster than its  $\alpha$  value, and it is tidally damped to Cassini State 2. The spin of Kepler-413b may also have free obliquity (not tidally damped), in which case the planet’s obliquity would precess around the binary axis with a period of  $\sim 300$  yr.

IOP Publishing sincerely regrets these errors.

<sup>12</sup> NASA Earth and Space Science Graduate Fellow.

<sup>13</sup> Hubble Fellow.